

DEVELOPMENT OF A METHOD FOR THE STUDY  
OF MECHANICAL PROPERTIES OF  
BRANCHED BLOOD VESSELS

by

Subhasis Behera

A thesis submitted to the faculty of  
The University of Utah  
in partial fulfillment of the requirements for the degree of

Master of Science

Department of Mechanical Engineering

The University of Utah

May 2013

Copyright © Subhasis Behera 2013

All Rights Reserved

# The University of Utah Graduate School

## STATEMENT OF THESIS APPROVAL

The following faculty members served as the supervisory committee chair and members for the thesis of \_\_\_\_\_Subhasis Behera \_\_\_\_\_.

Dates at right indicate the members' approval of the thesis.

\_\_\_\_\_Ken Monson\_\_\_\_\_, Chair 1/9/13  
Date Approved

\_\_\_\_\_K. Larry DeVries\_\_\_\_\_, Member 1/10/13  
Date Approved

\_\_\_\_\_Andrew Merryweather\_\_\_\_\_, Member 1/9/13  
Date Approved

The thesis has also been approved by \_\_\_\_\_Timothy Ameal\_\_\_\_\_ Chair

of the Department/School/College of \_\_\_\_\_Mechanical Engineering\_\_\_\_\_

and by Donna M. White, Interim Dean of The Graduate School.

## ABSTRACT

Defining the biomechanics of human cerebral vasculature is an important step towards a complete understanding of traumatic brain injury. This is, however, very difficult, because of the complex structure of cerebral arteries. One of the factors that enhances the complexity of the arteries is the high level of branching observed in them. The effect of the branching on the mechanical properties of the arteries is unknown. Previous efforts to define the influence of branches have been hampered by difficulties with test setup and a single camera view of specimen deformations. This work focused on overcoming these challenges but also implemented a number of general improvements to the current testing system. In particular, hardware and software changes were made to the existing test setup to synchronize video and data acquisition. A fixture has also been designed to simplify the branch test setup, and a dual camera system has also been integrated with existing hardware and software to provide for full three-dimensional (3D) evaluation of specimen motion. A three-dimensional Direct Linear Transformation (DLT) approach was designed to reconstruct the deformation of a branched blood vessel during isolated testing. These advancements were tested on a rat femoral artery with a prominent branch. The results suggest that the model can be successfully used to study human branched cerebral arteries.

## TABLE OF CONTENTS

ABSTRACT.....	iii
LIST OF FIGURES.....	vi
LIST OF TABLES.....	viii
ACKNOWLEDGEMENTS.....	ix
Chapters	
1. INTRODUCTION .....	1
1.1 Cerebral blood vessel injury.....	1
1.2 Branched cerebral arteries.....	2
1.3 Organization of the report.....	4
2. EXPERIMENTAL SETUP.....	5
2.1 Hardware.....	5
2.2 Software (LabVIEW) developments .....	8
2.2.1 Configure and display live video from one or two cameras.....	11
2.2.2 Synchronized image acquisition with the data acquisition.....	13
2.2.3 Vessel diameter measurement using image processing.....	15
3. BRANCHED VESSEL TESTING.....	24
3.1 Branched vessel test setup.....	24
3.2 Specimen preparation.....	26
3.3 Mechanical testing .....	27
3.4 Data processing and analysis.....	28
3.5 DLT camera calibration.....	29
3.5.1 Adaptation of DLT method in the experimental setup.....	29
3.5.2 Calibration object.....	31
3.5.3 Testing the DLT system.....	32
3.6 Experimental verification.....	34

4. SUMMARY AND FUTURE GOALS.....	48
REFERENCES.....	50

## LIST OF FIGURES

2.1	The dual platform linear stage in the vertical orientation.....	18
2.2	Schematic drawing of the test fixture showing different components.....	18
2.3	Schematic diagram of the test setup.....	19
2.4	The test setup user interface controls .....	20
2.5	The front panel when two cameras are selected .....	20
2.6	A string with its edges detected along the line overlaid by the user.....	21
2.7	Front panel showing the image processing parameter selection menu.....	22
3.1	Branched vessel test setup.....	38
3.2	Diagrammatic representation of the branched vessel test setup.....	38
3.3	Branched vessel test setup showing the two cameras during a test.....	39
3.4	Branched vessel support arm fixture with the vessel attached.....	39
3.5	(a) Drawings of the fixture.....	40
3.5	(b) Drawings of the fixture.....	41
3.6	Diagrammatic representation of rat femoral arteries.....	42
3.7	Object frame (XYZ-system) and image system (UV-system).....	42
3.8	Drawing of the calibration object with the dimensions in millimeters.....	43
3.9	Linear DLT experiment schematic.....	43
3.10	Rotational DLT experiment schematic.....	43
3.11	Calibration object kept on an adjustable protractor from Camera1.....	44

3.12	Calibration object kept on an adjustable protractor from Camera2.....	44
3.13	Proposed cross-section of the calibration object.....	45
3.14	Rat femoral branched blood vessel.....	45
3.15	Calibration object (a) cam1 Image (b) cam2 Image.....	46
3.16	The points marked by the microspheres traced for the strain measurements...	46



## LIST OF TABLES

2.1	Sample data logging file, highlighting the image counter column.....	23
3.1.	Results of the linear DLT experiment .....	47
3.2	Results of the rotational DLT experiment .....	47
3.3	Stretch ratios $\lambda_x, \lambda_y, \lambda_z$ for the above five pairs of points in Figure 3.16.....	47

## ACKNOWLEDGEMENTS

I would like to thank Dr. Ken Monson for his guidance and support throughout my research. I would also like to thank Dr. DeVries and Dr. Merryweather for their support.

## CHAPTER 1

### INTRODUCTION

Traumatic Brain Injury (TBI) is responsible for the death and disability of many children and adults. It can result from a number of sources including accidents, violence, sports and exposure to blast, which lead to a head injury usually causing damage to the blood vessels. This study attempts to develop a method to investigate the mechanical behavior of the vulnerable locations of a blood vessel under stretch.

#### 1.1 Cerebral blood vessel injury

TBI is caused when an external force injures the brain by a direct impact, rapid acceleration, blast waves, or penetration by a projectile [15, 16, 17, 18]. The cerebral blood vessels are often damaged resulting in intracranial bleeding, which in turn leads to the other pathophysiology of the brain. So, understanding the mechanical properties and the mechanical limits of the cerebral blood vessels is essential for understanding TBI. Prior work has been done by researchers [1, 2] to study and characterize the axial properties of fresh human cerebral arteries. This study [1] has shown that, “arteries are considerably stiffer than veins, carrying approximately twice as much stress at failure but withstanding only half as much stretch.” This suggests that the arteries are more prone to failure under a defined displacement. The cerebral arteries are very highly

branched and it has been hypothesized that branch points are particularly susceptible to injury. Their effect on the mechanical properties of the arteries is unknown. Previous efforts at testing the influence of branch points in our lab have been hampered by the lack of suitable fixture to secure a branched vessel and by the visualization of vessel deformations in just one plane. Because of the complex geometry of the branch, it is necessary to characterize its motion in three dimensions to fully evaluate its deformation. This thesis aimed to overcome these challenges.

### 1.2 Branched cerebral arteries

The effect of branching on the blood flow of cerebral vessels has been studied by researchers [4, 5]. However these works are focused on the blood flow only and do not speak about the mechanical properties of branched arteries themselves. There is only one study of branched cerebral vessel mechanics, in which 85 specimen were prepared from cerebral arteries (46 branched and 39 unbranched) obtained from cadavers and were subjected to bursting pressure tests [3]. This study showed that the branched specimens ruptured at a lower mean pressure of 1.574 bar compared to unbranched specimens, which ruptured at mean pressure of 2.172 bar. Even though the study clearly shows the vulnerability of branched cerebral vessels qualitatively, it does not give a clear quantitative relationship between pressure and deformation at the branch points, relative to the unbranched section.

Due to the very small size and fragile nature of the arteries, video strain analysis is the only viable method for the strain deformation analysis. In this method, the strain is measured by tracking deformation of the object under investigation in its images taken

during the experiment. There are two ways of tracking the deformation on the specimen. One is tracking some naturally existing distinct features on the surface of the specimen and another is to artificially place markers on the surface that can be tracked. Researchers have used polarized light to enhance the contrast of soft tissue (aortic valve) by exposing its collagen fibers, and used those enhanced features in the images to track deformation [11]. However the limitation of this method requires a single thin layered specimen for the transmission of polarized light. The more conventional approach is to use microspheres on the surface of the specimen and those microspheres are tracked in the images to calculate the deformation. Applying this method with a single camera gives very good results for deformations that remain within the plane perpendicular to the camera view, such as axial strain measurements of an unbranched vessel. However, the single camera method is prone to several kinds of errors, the most fundamental of which is the inability of the camera to track particle motion perpendicular to the plane of focus. Another problem arises when the camera is not parallel to the area of observation; the resulting image does not have the same scale throughout. As a result, measurements made do not have the same proportionality to the actual size of the object throughout the image. In order to have a good look at the branch location, the camera has to be usually kept in a nonparallel position with respect to the vessel. All these errors make it impossible to perform accurate strain measurements of a branch location using one camera. To overcome this problem we used the 3D Direct Linear Transformation (DLT) method to reconstruct the motion of the particles on the specimen. Everett [7] has implemented this two camera DLT method to study mechanics at the arterial bifurcation. The DLT method converts two

sets of two-dimensional (2D) camera pixel coordinates into a single set of 3D coordinates. Since the specimen is deformed during the experiment, both the cameras need to be synchronized to give accurate results. This work is focused on designing a test setup with synchronized image acquisition from two cameras and implementing the DLT method to reconstruct the deformations of the sample.

### 1.3 Organization of the report

Chapter 2 discusses about the data acquisition hardware and the user-interface and control software of the test setup. The modifications made to the software of the test setup during this work are discussed in detail.

Chapter 3 discusses about the mechanical test fixture and the test procedure. The implementation of DLT method in branched vessel testing is also discussed in this section. The accuracy of DLT method is examined in a controlled test. A branched section of a rat femoral artery is experimented on using the test setup. The results of this test and the limitations of the procedure and equipment are discussed.

Chapter 4 summarizes the results of the work and discusses the limitations of the current system. The future improvements needed in the system for more accurate results are discussed.

## CHAPTER 2

### EXPERIMENTAL SETUP

This chapter describes the test setup, which includes the data acquisition hardware, the user-interface and control software. During this work, some modifications were made in the user-interface software with the objective to make it more user-friendly and efficient while making it less prone to user errors. Some new features were added to the software to make the data acquisition more accurate and reduce the post processing time to analyze the data. The following sections describe these modifications in detail.

#### 2.1 Hardware

The mechanical testing was done using an existing test setup, on which the blood vessel is mounted and then pressurized and stretched at controlled rates. A dual platform linear stage (Parker Automation), driven by a stepper motor, is used to produce the axial stretch. The linear stage can be used in vertical or horizontal orientation. Figure 2.1 shows the departing motion of the platforms. Both platforms can depart or approach each other based on the rotational direction of the stepper motor. This motion is transferred to the blood vessels by attaching them to the platforms by appropriate fixtures. The user interface of the test setup is programmed in LabVIEW. I have made some modifications and added some new functionalities in existing user interface

software to improve the accuracy to the tests and reducing the post processing time, which will be discussed in this section. The software has the following three main functionalities.

- Control the devices by sending commands selected by the user.
- Configure, collect and display data from all sensors.
- Configure, Collect and display images from one or two camera

Figure 2.2 shows the schematic representation of the blood vessel connected to the linear stage. Both ends of the vessel segment are tied using silk suture to grooved, luer hub needles attached to acrylic blocks. These acrylic blocks have through holes, which allow fluid passage. The upper acrylic block is attached with an 11 N load cell (Transducer Techniques, MDB 2.5) which is attached to Platform 1 of the stage. The lower acrylic block is directly attached to the Platform 2. A clear plastic bath is attached to the lower acrylic block which is filled with saline solution surrounding the blood vessel. A digital video camera (Pixelink, PL-A641) fitted with a zoom lens (Edmund Optics, VZM 450i), capable of being triggered externally by a digital trigger, is used to monitor the specimen. Saline solution can be pushed into the blood vessel through the drilled lower acrylic block by a syringe attached to a linear actuator (Ultramotion, Digit). Inline pressure transducers (Honeywell, MicroSwitch 26PCDFM6G) are attached to both the input and output pressure line, equidistant from the vessel. The internal vessel pressure is calculated as the average of these two pressure transducer readings. The displacement of the linear stage is measured with a digital encoder (resolution 1.0  $\mu\text{m}$ ) attached to the stepper motor. Data acquisition from the pressure transducers, load cells, digital encoders and video acquisition, as well as control of the



test set-up, is done by National Instruments hardware-based data acquisition and control modules and is programmed in LabVIEW.

The test setup consists of the following data acquisition and control components.

- SCXI-1600 (USB data acquisition and control module)
- PCI-6602 (timing and digital I/O module)
- PCI-7334 (4-axis stepper motor control module)
- GPIB (General Purpose I/O Bus) module based external devices.

The SCXI-1600 module is a USB data acquisition device with a 16-bit ADC. It collects data from analog sensors like pressure transducers, and load cells and digitizes the data and sends it through a USB port. The PCI-6602 is a counter/timer module and is used to collect data from encoders to record the motion of the stepper motors. These two devices are synchronized by using one of the two programmable function input (PFI) pins of the SCXI-1600 as shown in Figure 2.3. The PFI 0 pin of the SCXI-1600 is configured as a sample clock for the PCI-6602. The PCI-6602 reads the encoders in every clock cycle as governed by the PFI0 input from the SCXI-1600. Thus these two devices are synchronized. The same timing clock is used to create a digital pulse that is used to trigger the cameras. This will be discussed in detail in the next section.

PCI-7334 is a stepper motor controller, which can control up to four stepper motors. In our test setup we use the PCI-7334 to control three stepper motors. Two of these motors produce the pull motion in the blood vessel and its branch. Digital Encoders are mounted on these two stepper motors, which give information about the motion of the needles on which the blood vessel is mounted. The third stepper motor is used to drive

the linear actuator which controls the syringe that produces pressure in the blood vessel. The motors are controlled using the motion control DLLs of LabVIEW.

The stepper motors and the GPIB based devices are used to exert the controlling motion and pressure in the system. GPIB communication is used to communicate with the following devices:

- A voice coil linear actuator
- A flow controller
- A pressure controller.

The voice coil is used to produce rapid motion in the system. This actuator was not used in the current system but can be used in future experiments to see the effect of rapid stretch. The flow meter and pressure meter are used to generate circulation pressure in the blood vessel.

## 2.2 Software (LabVIEW) Developments

The user interface of the test setup is programmed in LabVIEW. I have made some modifications and added some new functionality in existing user interface software which will be discussed in this section. The software has the following three main functionalities.

- Control the devices by sending commands selected by the user.
- Configure, collect and display data from all sensors.
- Configure, collect and display images from one or two cameras.

The front panel can be broadly divided into three main sections according to the three functionalities described above as outlined in Figure 2.4. Following is a detailed

description of the above functionalities. The features that will be discussed here were preexisting in the user interface software, unless stated explicitly as developed during this work.

Section 1 in Figure 2.4 contains the control inputs to control all the devices in the test setup except the two cameras. The top section named as “Jog Control” contains the control inputs to manually move the four actuators of test setup. The user can input displacement and velocity inputs and select a direction of motion of the actuators. Those controls are

- Daedel: These inputs correspond to the manual control of the dual platform linear stage.
- VC: These inputs correspond to the manual control of the voice coil actuator.
- NB: These inputs correspond to the manual control of the second linear stage.
- Digit: These inputs correspond to the manual control of the linear actuator-driven syringe used to create pressure.

The controls under the “Program Selection” section of the front panel lets the user select and characterize the predefined mechanical tests to run on the specimen and to select a file to save the data collected during the test. I have added functionality in this section to protect the data to be overwritten accidentally. The button to execute the test grays out and gets disabled after a test is completed. It stays disabled and does not let the user run a test until the user presses the OK button located to the right of the file selection control. This is to remind the user to select a new file to save the data collected

during the test, which in turn protects the data from being accidentally overwritten. The control logic of this functionality is as follows:

- Added a sequence to the end of every mechanical test
- Disabled and grayed out the EXECUTE button in the last sequence after the test has successfully completed
- Added an event case that is triggered when the OK Button is pressed. When this event occurs, it enables the EXECUTE button.

The “Program Parameters” section houses the parameters to be selected for the mechanical tests. These determine the test duration and extremities like in vivo pressure, minimum pressure, maximum pressure, minimum position (stretch), in vivo position, maximum position (stretch), velocity of stretching etc.

“DAQ Timing” section contains three controls that control the data acquisition rate. HS Samp Rate determines the sampling rate of the high speed tests. Sample Rate determines the rate for non-high speed tests. Samps/Chan controls the length of buffer to be held by the data acquisition system.

Section 2 in Figure 2.4 contains the feedbacks from the different sensors and encoders. The “Position Outputs” section contains the feedback from the linear stage and voice coil actuator’s position feedback based on their encoder readings. The graph located to the right of the “Position Outputs” section plots of the position outputs of the dual platform linear stage and either one of the voice coil actuator or the single platform linear stage depending on whichever is selected. The “VC/MB Pos (mm)” button to the left graph lets the user toggle between voice coil actuator and single platform linear stage.

The “Force/Pressure Outputs” section contains the readouts of all the pressure sensors and load cells of the system. These can be plotted in the graph adjacent to it. The user can select which signals to plot in the graph by clicking on the LED switches. These switches light up the LEDs, representing the signal are being displayed in the graph.

Section 3 of the front panel contains the camera display and the buttons which are used to control the camera. This section was completely developed as a part of this work, which has the following three functionalities:

- Configure and display live video from one or two cameras
- Synchronized image acquisition with the data acquisition
- Implementing an image processing method to calculate and plot the diameter of the blood vessel live during an experiment.

### 2.2.1 Configure and display live video from one or two cameras

This section discusses the video acquisition section of the front panel program. The video acquisition is programmed using NI-IMAQdx dynamic link libraries (DLLs). The application programming interface of NI-IMAQdx offers two kinds of image acquisition modes; buffered acquisition mode and triggered acquisition mode. The software is programmed to acquire images in the buffered acquisition mode to display the live video from the cameras in the front panel. When two cameras are used, the video from each camera can be viewed in the video display by using the drop down button which reads “Camera 1” and selecting the desired camera. This is done by using a case structure to pass the video feed from each camera into the video display window

and selecting the case by the above drop down button's output. The user is offered with controlling the exposure of the two cameras by using the control boxes "Camera 1 Exposure" and "Camera 2 Exposure". This control can change the exposure of the camera and can be used to enhance visibility of the image in case of low light condition. The "Select Path (Camera 1)" and "Select Path (Camera 2)" browse buttons lets the user, select a path to save the images. This path applies to both record and snapshot. The record option will be discussed in more detail in Section 2.2.2.

The buttons located at the top left of Figure 2.5 correspond to calibration of the images. This functionality was developed by another contributor to the program, which I integrated into the main program. However, this calibration process applies to the single camera mode testing configuration only. Direct Linear Transformation (DLT) method will be used for two camera branch tests, which will be discussed in Section 3.5.

The calibration of the single camera test configuration is done in the following steps:

- A small millimeter scale is carefully brought into the view field of the camera parallel to the vessel, such that the scale is at the same distance from the camera as the vessel.
- A still image of this is taken using the "Snapshot" button, which overlays on the top of the video, which will be used for the calibration process and gets automatically removed when the calibration process finishes.
- The "Calibrate Camera" button is pressed, which lets the user draw a line on the image using the mouse click-drag-click method. The user can draw a line

between two markings of the scale. The software then finds out the number of pixels included in the line.

- The user is then prompted to enter the number of units in millimeters encompassed by the line. The software then determines the relationship between pixels and millimeters and populates it in the “mm/pixel Value” indicator. This is stored in the program memory as well as in a text file in order to retrieve it later, if the software crashes in the middle of the test.
- The images are now calibrated and the ratio is written in the first row every file that is logged during the test.

When the user clicks the “Load Stored Calibration” button, the software reads the previously stored value of calibration from the file and updates the local variable, which carries the value of calibration ratio in the program run time. “Measure Vessel Length” button lets the user measure the length of the blood vessel by applying the calibration ratio. After clicking the button the user draw a line on the image using the mouse click-drag-click method, which is representative of the length of vessel. The software then finds out the number of pixels included in the line and finds out the vessel length by multiplying the calibration ratio with the number of pixels. “Vessel Length (mm)” indicator displays the above value.

### 2.2.2 Synchronized image acquisition with the data acquisition

The aim of this development was to synchronize the image acquisition with the data acquisition, so that each image could be directly associated with a corresponding data point. Instead of taking a video separately during the experiment, the image acquisition

was triggered by the data acquisition system in order to synchronize the camera with the data acquisition. The necessity for synchronized image acquisition is pronounced by the need to use two cameras for branched vessel testing, where both the images have to be taken simultaneously for greater accuracy of measurement.

As discussed in Section 2.1, the data acquisition devices SCXI-1600 and PCI-6602 are synchronized. The camera also has to be triggered at a rate synchronized with these data acquisition systems, so that each picture can be associated with a unique data point. However the maximum rate at which the cameras can acquire images is much slower than the data collection rate. Since the experiments take place at a slow rate, a high rate of image collection is not necessary. Hence a rate of three frames per second was selected as the rate at which to collect data in our experiments. Data collection takes place at a rate of 10000 cycles per second. So, one digital output pin of the PCI-6602 is programmed to toggle after every 3333 clock cycles, which is used to trigger the two cameras.

The digital trigger generation for the camera is controlled programmatically using the DAQmx function libraries and the image acquisition is programmed in LabVIEW using NI-IMAQdx function libraries, which are dynamic link libraries (DLLs). The digital triggering using the PCI-6602 is controlled using the DAQmx functions. The triggering is generated only when the record button is switched on and is stopped when the record button is switched off.

The application programming interface of NI-IMAQdx has two kinds of image acquisition modes; buffered and triggered acquisition mode. The software is programmed to acquire images in the buffered acquisition mode when the program runs



but the data is not being recorded. It acquires images and shows a live feed of the specimen. The trigger mode is activated, when the data recording is started and goes back to the buffer mode, when it is stopped. To match the image with the data acquisition, a variable image counter is used. It increments every time a new trigger is issued to the cameras and can be reset to zero manually. This value is written in a column of the data file with the image counter value repeating in each row till it is incremented since the data are logged at a much higher rate than image collection. Table 2.1 shows a part of the data file which illustrates this. Each image has the image counter associated with its name. The image name also includes the name of the test being performed, which eliminates the need to select separate folders for each test.

### 2.2.3 Vessel diameter measurement using image processing

An image processing application was developed to measure the diameter of the blood vessel while an experiment is taking place. This application uses an edge detection routine in LabVIEW to detect the edges of the blood vessel across a straight line overlaid on the image by the user. The edge detection function detects the grayscale intensity of the image along the line. Wherever there is more than the threshold change in intensity, as determined by the parameters chosen by the user, that point is marked as an edge. The user can adjust the parameters to assist in the edge detection as the image quality varies significantly with the lighting and even slight change of focus. Figure 2.6 shows the edge detection process.

Figure 2.7 shows the software front panel, when adjusting the parameters for edge detection. A string was used to simulate a vessel. The image processing algorithm

converts the image to a grayscale image before finding the edge. When the user draws a line on the image, and clicks on the Adjust Image Processing button, the front panel looks as shown in Figure 2.7. The plot on the bottom left side of the screen displays the grayscale values of the image along the line drawn over it. This is usually hidden from the front panel but is visible when the Adjust Image Processing button is selected.

The figure shows that there is a clear drop in the grayscale value across the edge. In a case like this, the edges will be easily picked up by the algorithm even with a large value of minimum edge strength, one of the required user-selected parameters. Sometimes, the image is blurry and the edges are not sharp enough. In that case, the user can adjust the parameters (encircled by the second red circle) like contrast and brightness and can observe the resulting changes in the plot. The user can then choose a suitable value of minimum edge strength so that the algorithm easily detects the edge.

The changes in the user interface software as discussed in this chapter streamlined the testing process and made it easier to perform the tests as well as the post processing of the data collected during the tests. The synchronization of the image acquisition with the data acquisition eliminated the need of doing that manually during the post processing of the data and thus saved a lot of time. The triggering of both the cameras simultaneously at the same rate was extremely essential for the accuracy of the two camera Direct Linear Transformation (DLT) method which will be discussed in Chapter 3. Integration of the calibration utility with the test-setup, helped to save a lot of post processing time. It also enabled measuring the real lengths of the different parts of the blood vessels easily. Finally the image processing based automatic axial diameter

measurement functionality enabled tracking the diameter during the tests for a prolonged period, which would have taken a lot of time to do manually.

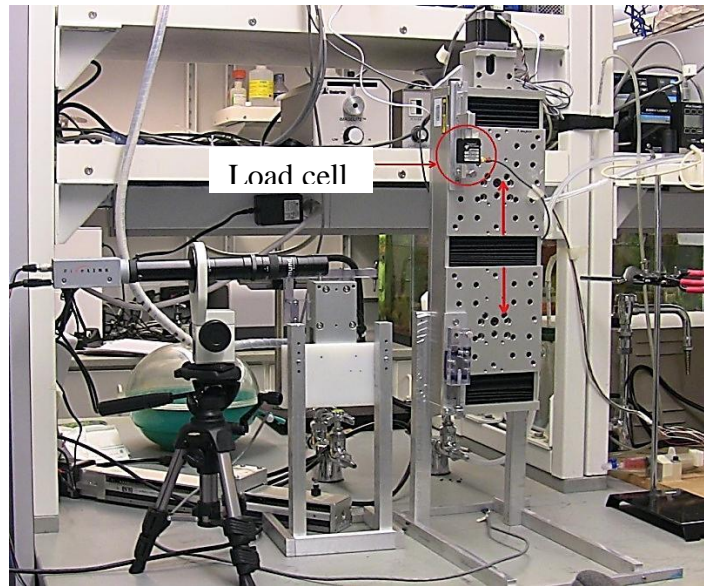


Figure 2.1. The dual platform linear stage in the vertical orientation

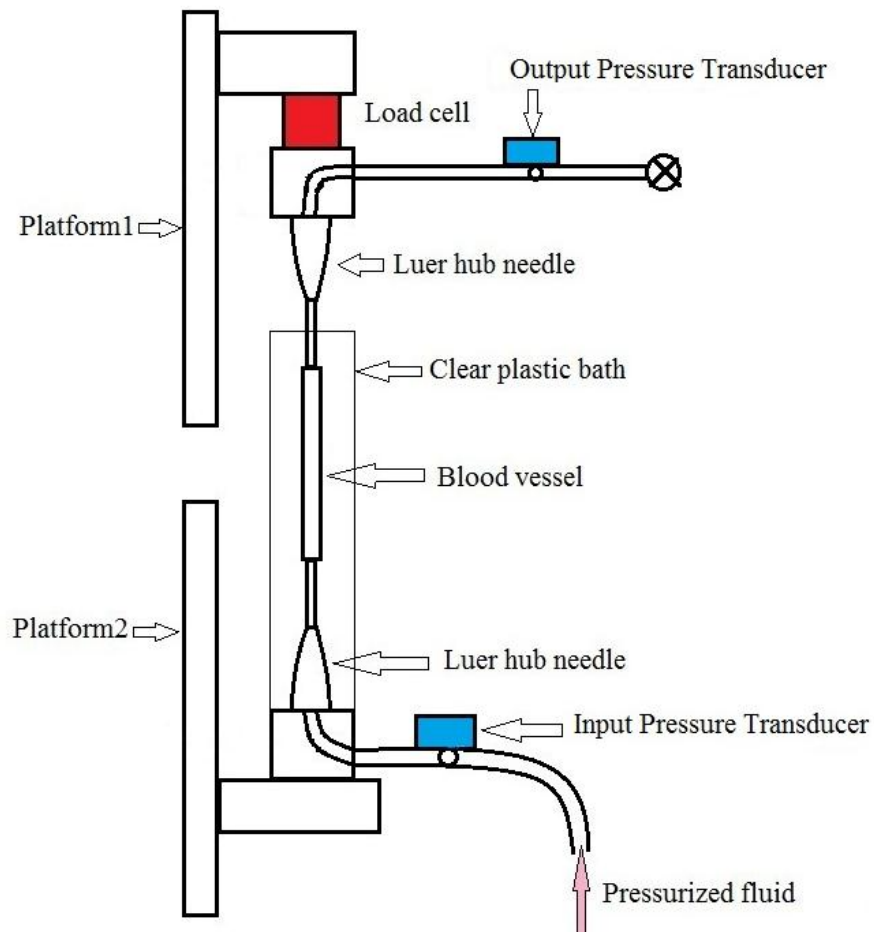


Figure 2.2. Schematic drawing of the test fixture showing different components

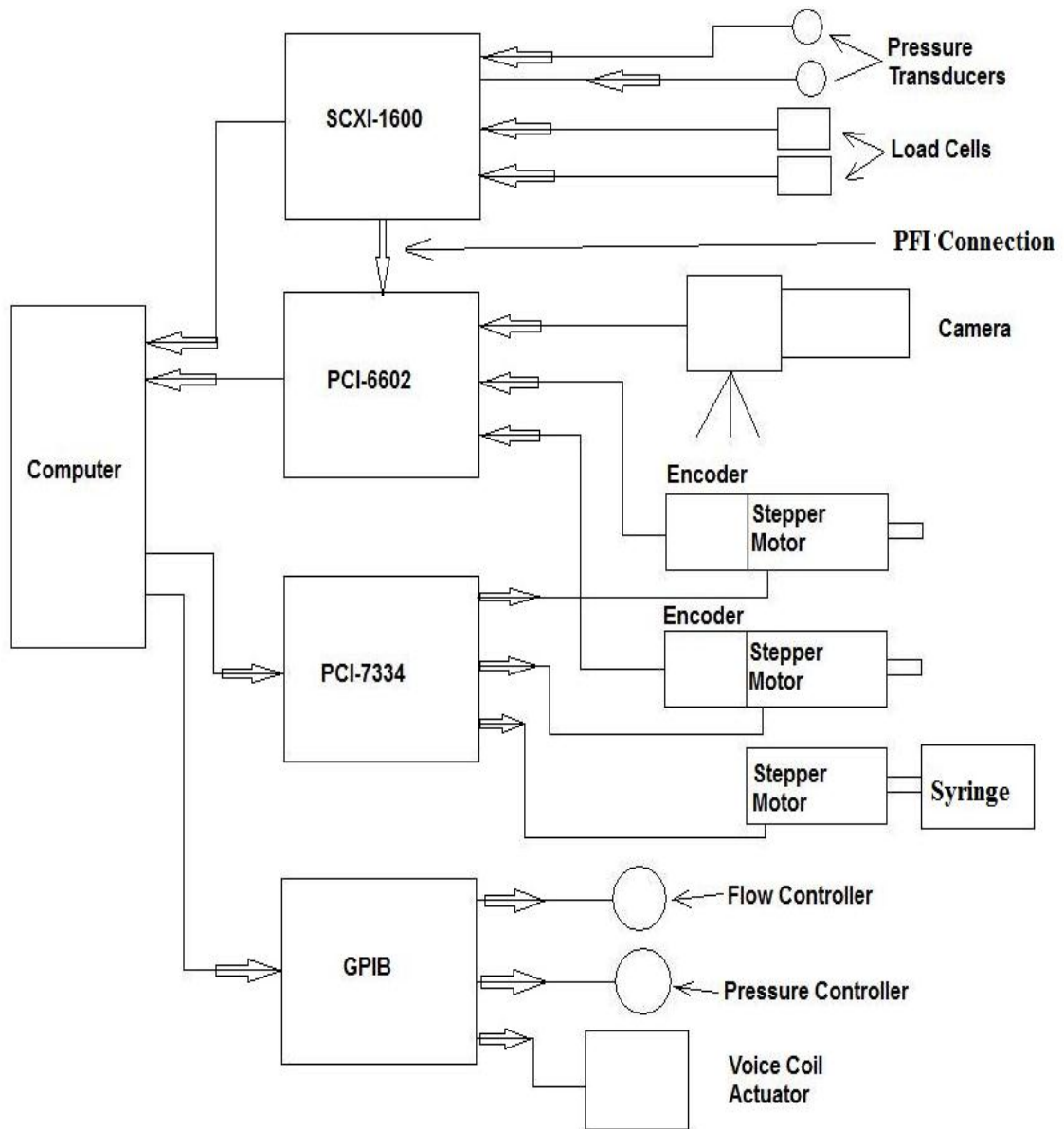


Figure 2.3. Schematic diagram of the test setup

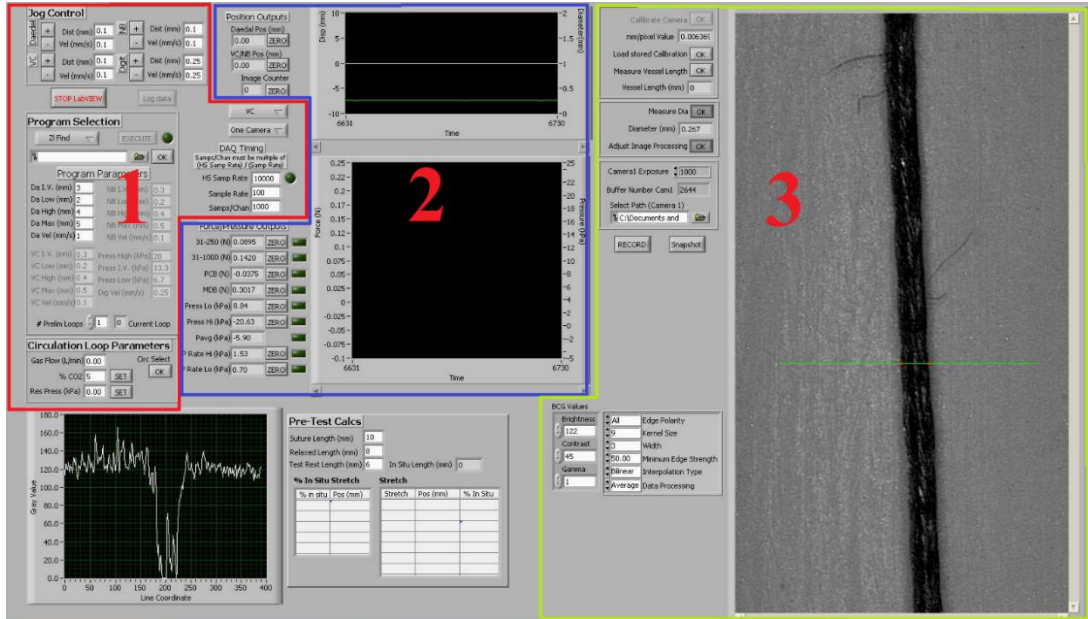


Figure 2.4. The test setup user interface controls

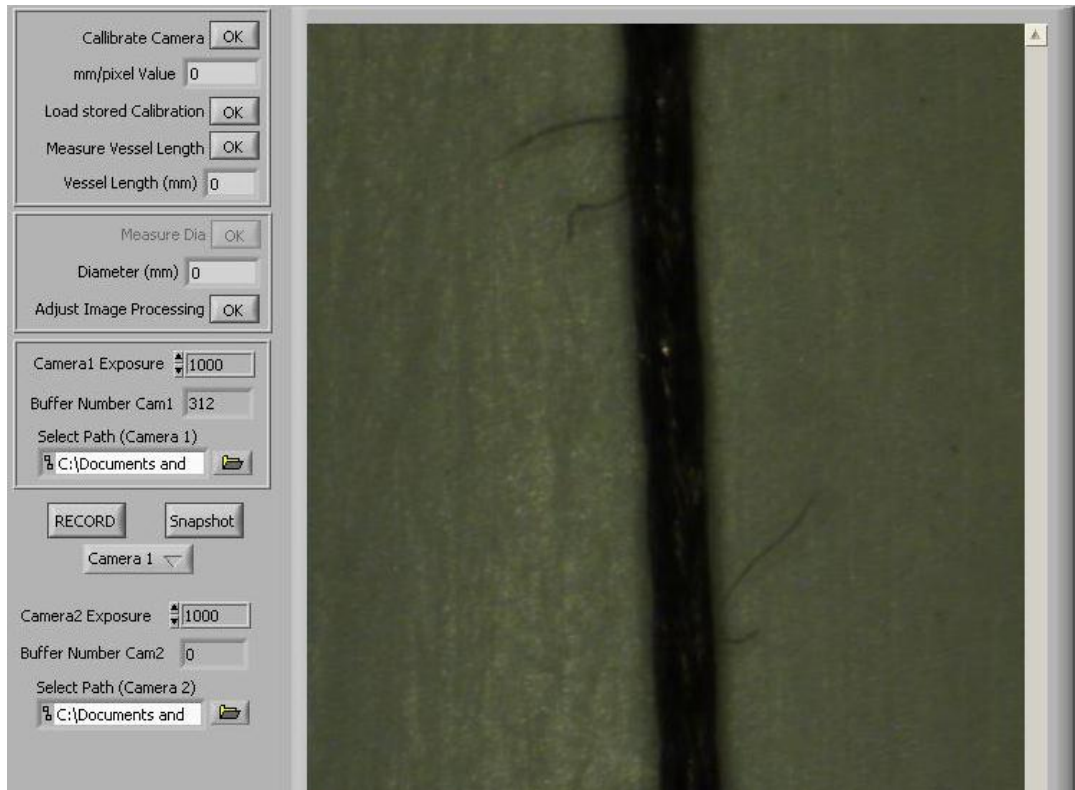


Figure 2.5. The front panel when two cameras are selected



Figure 2.6. A string with its edges detected along the line overlaid by the user





Figure 2.7. Front panel showing the image processing parameter selection menu



Table 2.1 Sample data logging file, highlighting the image counter column

511.13	0.3	0.270068	-0.02988	0.964634	32.93156	11.72418	22.32787	-0.03175	-0.00121	-0.00456	0.146546	4	0
511.14	0.3	0.271318	-0.03738	0.94962	32.78628	11.70522	22.24575	-0.03464	-0.00162	-0.00285	0.145154	4	0
511.15	0.3	0.271318	-0.03738	0.942113	34.22638	11.71786	22.97212	-0.02886	-0.00162	-0.00114	0.146464	4	0
511.16	0.3	0.272568	-0.03738	0.94962	31.93359	11.71154	21.82256	-0.0303	-0.00121	-0.00114	0.145727	4	0
511.17	0.3	0.272568	-0.03738	0.957127	34.18848	11.70522	22.94685	-0.03175	0.000404	0.001141	0.145809	4	0
511.18	0.3	0.273818	-0.02988	0.964634	32.91892	11.71786	22.31839	-0.03609	-0.00121	0	0.14671	4	0
511.19	0.3	0.275069	-0.03738	0.964634	32.76733	11.72418	22.24576	-0.03609	-0.00242	-0.00456	0.145236	4	0
511.2	0.3	0.275069	-0.0524	0.94962	34.22638	11.70522	22.9658	-0.02741	-0.00929	-0.00228	0.146301	4	0
511.21	0.3	0.276319	-0.03738	0.957127	31.96518	11.71786	21.84152	-0.0303	-0.00444	-0.00114	0.145809	4	0
511.22	0.3	0.277569	-0.03738	0.957127	34.20743	11.71786	22.96264	-0.0303	-0.00323	0.001711	0.145727	4	0
511.23	0.3	0.27882	-0.02988	0.94962	32.87471	11.72418	22.29944	-0.03464	-0.00121	-0.00285	0.146382	4	0
511.24	0.3	0.27882	-0.03738	0.934606	32.72944	11.71154	22.22049	-0.03464	-0.00081	-0.00342	0.145154	5	0
511.25	0.3	0.28007	-0.02988	0.957127	34.20111	11.71154	22.95632	-0.02886	0.002826	-0.00057	0.146546	5	0
511.26	0.3	0.28132	-0.02237	0.964634	31.93991	11.71154	21.82572	-0.03175	-0.00242	-0.00171	0.145809	5	0
511.27	0.3	0.282571	-0.0524	0.964634	34.18216	11.7305	22.95633	-0.02886	0.001211	-0.00114	0.145727	5	0
511.28	0.3	0.283821	-0.02988	0.957127	32.88103	11.71154	22.29628	-0.03754	0.002019	-0.00456	0.146546	5	0
511.29	0.3	0.286322	-0.02988	0.942113	32.74838	11.6989	22.22364	-0.03754	-0.0004	-0.00285	0.144908	5	0
511.3	0.3	0.287572	-0.02237	0.957127	34.20743	11.71786	22.96264	-0.02886	0.005249	0.001141	0.146464	5	0
511.31	0.3	0.288822	-0.02988	0.942113	31.90833	11.68625	21.79729	-0.03175	0	-0.00114	0.145645	5	0
511.32	0.3	0.290073	-0.02237	0.942113	34.13795	11.6989	22.91842	-0.02886	0.004037	0.001141	0.145727	5	0
511.33	0.3	0.291323	-0.02988	0.957127	32.8305	11.71786	22.27418	-0.03609	0.000404	0.001141	0.146464	5	0
511.34	0.3	0.292573	-0.02988	0.942113	32.66627	11.70522	22.18574	-0.03609	0.002019	-0.00342	0.14499	5	0

## CHAPTER 3

### BRANCHED VESSEL TESTING

This chapter describes the test setup and test procedure for the branched blood vessel testing. Some additional tools are required to do branched blood vessel testing accurately. The ability to mount the branched specimen onto the test setup and transfer it safely necessitated the design of a fixture. The need to see the curved regions of the branch location to estimate the stretch correctly necessitated using two cameras and a method to calibrate them. This chapter discusses the implementation of methods to achieve these objectives.

#### 3.1 Branched vessel test setup

The branched blood vessel mechanical testing requires changes in the original test setup (Chapter 2.1). The dual platform linear stage assumes a horizontal position. A second linear stage is used at an angle, which stretches the branch. Both ends of the main segment of branched blood vessel are mounted on the grooved needles of Arm1 and Arm2 (attached to the two platforms on the dual platform linear stage).

The branch segment is mounted on the grooved needle of Arm3 (attached to the second linear stage). As shown in Figure 3.1, an 11 N load cell (Transducer Techniques, MDB 2.5) is attached to Arm1, and a 9.8N load cell (Honeywell, model 31/1000) is

attached to Arm3. The blood vessel is connected to a saline delivery system through Arm2 which, apart from delivering saline solution, also creates static pressure in the blood vessel. This system is driven by a linear actuator, which creates pressure by pushing the syringe. A 200 kPa pressure transducer (Honeywell, MicroSwitch 26PCDFM6G) is used to measure the input pressure before the solution passes to Arm2. Since the test setup is horizontal, there is no pressure change due to gravity. Actuator displacement is monitored using quadrature encoders, and specimen deformations are recorded (3 frames/second) using 2 digital cameras (Pixelink, PL-A641) with attached high-powered zoom lenses (FOV: 1.4-17.6 mm; Edmund Optics, VZM 450i). The two cameras are placed at oblique angles such that they can have a clear view of the branch, as shown in Figure 3.3. The images from the two cameras can be used to reconstruct the 3D coordinates of the viewed region using the DLT method (Section 3.5). It was difficult for the cameras to maintain balance on tripods at the selected angles, so the tripod supporting Camera1 was secured to the wall and Camera2 was placed on a vacuum suction cup-based camera mount (Delkin, Fat Gecko).

Before attaching the arms to the actuators, the vessel first needs to be attached to the needles on the arms under the microscope. The size and configuration of branched vessels vary, so the positions of the arms need to be adjustable relative to each other. A fixture was designed for this purpose which can not only facilitate attaching the branched vessel securely on to the needles, but also help to move the branched vessel needle assembly to the test setup without causing any damage to the vessel. Figure 3.4 displays a picture of the fixture, with a branched vessel mounted on it. The fixture has 3 degrees of freedom to manipulate the location of the three arms and 1 degree of

freedom to translate the whole assembly up and down using three supporting legs. Arm1 can be translated along its axis as shown in Figure 3.4. Arm3 has two degrees of freedom. It can be swung around along the disc to allow the branch to be attached at its natural angle. It can also be translated along its axis to allow for the variation of the length of the branch. The three supporting legs help to adjust the height of the whole assembly which is necessary both while placing the assembly under the microscope so that the needles are submerged in the saline solution as well as while attaching the arms to the stage so that the arms line up with the stage correctly. Figure 3.5 shows the drawings of the swinging arm and the disc respectively, which were fabricated for this experiment.

### 3.2 Specimen preparation

A rat femoral artery was dissected from a previously euthanized, male Sprague Dawley rat, conforming to the standards established by the Institutional Animal Use and Care Committee at the University of Utah. Rats were sacrificed by exposure to an overdose of CO<sub>2</sub>. Then a section of the femoral artery was dissected and placed in saline solution. Figure 3.6 shows a diagrammatic representation of the femoral artery in the rat body.

The dissection was performed such that it contained a section of the femoral artery which had a large branch. The specimen also included some small branches which were tied off using a single fibril of unwound 6-0 silk suture. Both ends of the main vessel segment and the branch were tied using 6-0 silk suture to grooved, luer-hub needles attached to the described arms. After attaching the branched artery to the three arms under the microscope, the specimen was removed from the saline bath and dried by

gently touching it with a piece of Kim Wipe. A small amount of cyanoacrylate (super glue) was then applied around the vessel-needle interfaces on the distal sides of the sutures to seal the vessels. To enhance the visibility of deformation on the surface of the arteries, 10  $\mu\text{m}$  dried black polystyrene microspheres (Polysciences, Inc.; Polybead) was applied on the surface of the artery using a prong of a pair of micro forceps. The microspheres stick to the surface of the artery by getting caught in the rough adventitial layer of the artery. Special care was taken to apply microspheres with a higher concentration at the branch location. The microspheres make it easier to track the surface deformations from the images collected during mechanical testing. The specimen was then carefully carried to the test set up, while being mounted on the fixture. The fixture ensures that the specimen is undamaged during the transfer. To attach the arms to the actuators in the test setup, the fixture was flipped and the arms were placed in their respective attachment positions. The arms were attached to the linear actuators, as described in Section 3.1, immersing the specimen in the saline bath as shown in Figure 3.1. The fixture was then disconnected from the arms and removed.

### 3.3 Mechanical testing

When the blood vessel is dissected from the rat, structural rearrangement took place in it because of the removal of the natural pressure and load it had in its in vivo state. The blood vessel needs to be brought close to its in vivo state by a preconditioning process before performing mechanical tests on it. The main section of the blood vessel is stretched axially to its in vivo length and held there. The branched section is stretched to a selected length, guided by the in vivo length and held constant while pressure in the vessel was cycled four times between 6.7 and 20 kPa. In each successive

preconditioning test the axial stretch was gradually increased until there was significant variation in force (approximately 0.1 N) with the variation in pressure. The stretch value at which this occurred was 0.6 mm. The vessel length was held at in vivo length and the pressure at 13.7 kPa between each preconditioning test. After the preconditioning tests, the pressure was held at 13.7 kPa and the branch was subjected to four cycles of stretch varying between selected high (0.6 mm) and low values (0.2 mm) followed by stretching to a maximum length (1.1 mm) which was expected to cause failure of the branch. Branch failure did not occur in the experiment conducted. However the goal of this experiment was to demonstrate use of the developed specimen preparation fixture and the utility of the DLT method; the deformations obtained were considered to be sufficient.

### 3.4 Data processing and analysis

Data from the two load cells, the pressure transducer, the actuator motion and the images from the cameras were recorded in a file. Only the image data were evaluated to meet the objectives here. Images representing the reference and maximum deformation configurations were then identified. The reference image was defined as the image corresponding to the unloaded vessel length, and the maximum deformation was the last image collected.

The recorded data were used to compute the maximum stretch value. Stretch ratios

$\lambda_x, \lambda_y, \lambda_z$  are defined in Equation 1,

$$\lambda_x = \frac{X_{F,i} - X_{F,j}}{X_{R,i} - X_{R,j}}$$

$$\lambda_y = \frac{Y_{F,i} - Y_{F,j}}{Y_{R,i} - Y_{R,j}}$$

$$\lambda_z = \frac{Z_{F,i} - Z_{F,j}}{Z_{R,i} - Z_{R,j}} \quad (1)$$

where,  $X$ ,  $Y$ ,  $Z$  are the coordinates of microsphere  $i$  or  $j$  in either the reference,  $R$ , or final,  $F$ , configuration. Since the branched vessel stretch cannot be confined to one plane, let alone one axis, as opposed to axial stretch, it is essential to obtain the 3D coordinates of the points of interest to calculate the stretch more accurately. Through the application of DLT, the 3D coordinates of selected points were obtained from the 2D images from two cameras.

### 3.5 DLT camera calibration

The method to compute the real world 3D coordinates of the blood vessel using images from two cameras will be discussed in this section. The Direct Linear Transform (DLT) [7, 8] system was used to calibrate the cameras. The accuracy of the DLT method will be experimentally verified.

#### 3.5.1 Adaptation of DLT method in the experimental setup

DLT is a camera calibration method first used by Karara [7] and is commonly used in systems having multiple cameras. The DLT method for two cameras requires a set of known control points. The control points are normally fixed to a rigid frame, known as

the calibration object. The images of this calibration object are taken by both the cameras. The goal is to determine the mapping between the 2D coordinates of the local/image reference frame and the 3D coordinates of the global/calibration object reference frame. This mapping relationship can then be used to reconstruct the real world 3D coordinates of points in the object of interest from the known 2D coordinates of the image from each camera. This is diagrammatically shown in Figure 3.7. The following is a description of application of the DLT calibration method in a two camera system.

Let us assume that the image coordinates of a point in the images corresponding to Camera1 and Camera2 are  $[u_1, v_1]$  and  $[u_2, v_2]$  respectively, and the real world 3D coordinates are  $[x, y, z]$ . The coefficients  $L_1, L_2, L_3 \dots L_{11}$  are the DLT parameters, which establish the relationship between the object coordinate frame and the image coordinate frame. Each camera has its own DLT parameters. In equation 2 [26], the superscript associated with the DLT parameters denotes the camera number. The real world 3D coordinates can be reconstructed from the image coordinates by using the following relationship.

$$\begin{bmatrix} \frac{u_1 L_9^1 - L_1^1}{R^1} & \frac{u_1 L_{10}^1 - L_2^1}{R^1} & \frac{u_1 L_{11}^1 - L_3^1}{R^1} \\ \frac{v_1 L_9^1 - L_5^1}{R^1} & \frac{v_1 L_{10}^1 - L_6^1}{R^1} & \frac{v_1 L_{11}^1 - L_7^1}{R^1} \\ \frac{u_2 L_9^2 - L_1^2}{R^2} & \frac{u_2 L_{10}^2 - L_2^2}{R^2} & \frac{u_2 L_{11}^2 - L_3^2}{R^2} \\ \frac{v_2 L_9^2 - L_5^2}{R^2} & \frac{v_2 L_{10}^2 - L_6^2}{R^2} & \frac{v_2 L_{11}^2 - L_7^2}{R^2} \end{bmatrix} \begin{bmatrix} x \\ y \\ z \end{bmatrix} = \begin{bmatrix} \frac{L_4^1 - u_1}{R^1} \\ \frac{L_8^1 - v_1}{R^1} \\ \frac{L_4^2 - u_2}{R^2} \\ \frac{L_8^2 - v_2}{R^2} \end{bmatrix} \quad (2)$$



### 3.5.2 Calibration object

The implementation of DLT calibration in the two camera experimental setup will be discussed in this section. One of the most important things in the accuracy of DLT reconstruction method is an appropriate calibration object. The calibration object should have the following characteristics.

- For the 3D DLT method to work correctly, a 3D calibration object has to be used. In other words the calibration object should have control points representing changes in all the three dimensions.
- The calibration object must be large enough to include the entire space of motion. If its size is not adequate, the mapping between the 2D coordinates of the local/image reference frame and the 3D coordinates of the global/calibration object reference frame may not be accurate. If a part of the test specimen lies outside the area covered by the calibration object, the DLT method will extrapolate to get the 3D coordinates, which is more prone to error.
- The larger the number of control points, the more accurate the results, so the calibration object should have a sufficient number of control points. In a two camera setup the minimum number of control points required is 6. However using about 10 control points gives a more accurate prediction.

Even though 3D DLT is very common in large scale motion analysis, it is not very common in the scale that we were measuring the motion. It is mainly because of the difficulty associated with constructing a miniature 3D calibration object. Even though 2D calibration grids are available in several sizes commercially, no calibration object

was found in the size that was required in the branched vessel test experiments. So we designed a calibration object in our lab according to the needs of our experiments and satisfying the above guidelines. Figure 3.8 shows the drawing and dimensions of the calibration object. Each vertex of the calibration object can be used as a control point. So the shape of the calibration object had to have a large number of vertices. However they will only be usable if the vertices lie in more than one plane and could be visible from multiple camera angles simultaneously. So they need to be sufficiently separated to allow visibility. Because of these competing demands, the following shape was arrived at as a middle ground.

### 3.5.3 Testing the DLT system

Since the accuracy of DLT reconstruction depends on the control points on the calibration object and the accuracy of the measurements, it was necessary to test the DLT system to verify that it predicts correct results. Two experiments were designed to test the accuracy of the results in translation and rotation motions.

Figure 3.9 shows the schematic representation of translation experiment. The calibration object is translated a known distance on a linear actuator whose resolution is based on a digital encoder with resolution of  $0.1 \mu\text{m}$ . The DLT parameters for both the cameras were computed in the first location and the DLT reconstruction was applied to predict the 3D locations of the points in the subsequent locations. Then these results were compared with the actual 3D locations of the calibration object. Table 3.1 summarizes the results of this experiment.

Figure 3.10 shows a schematic representation of the rotational experiment. The calibration object was placed on an adjustable round steel protractor (General Tools) with a resolution of 1 degree and rotated by a known angle. The DLT parameters were computed in its first position and DLT reconstruction was applied to predict the 3D locations of the rotated calibration object. Table 3.2 summarizes the results of this experiment.

From Tables 3.1 and 3.2, it is clear that the DLT reconstruction works quite accurately in X and Y axes. However, the results in the Z axis do not predict as accurately as in the X and Y axes. This is because there were very few control points in the Z direction and the total span of points in Z axis was very low. The reason why a smaller span in Z axis causes the DLT estimation of the points to be more inaccurate is the following. The above experiment was prone to an inherent noise in measurement. It is introduced by the small inaccuracies in locating the markers in the 4 images, which depends upon the clarity of the image and the ability of the analyst to accurately identify the marker locations in the images. The effect of this factor is enhanced if the total span of the points in the axis is low. For example in the above calibration object the total spread in the Z axis was 2 millimeters. So a smaller inaccuracy in the estimation of the position, which may result from the error in identifying the markers' locations, could cause a larger error percentage in position estimation using DLT method. The accuracy of the results could increase,

- If a more accurate calibration object would be used. The edges and vertices of the calibration object should be sharper. One way to achieve this could be by using laser machining to build the calibration object.

- It also should have more calibration points in all the dimensions. The current calibration object has vertices only in two vertical planes. An object with more vertices in Z direction will enhance the accuracy of the Z direction measurements. For example, the surface cross-section of the calibration object parallel to the Z direction could be a stepped rectangle as shown in Figure 3.13, instead of being a simple rectangle. However, this will enhance the complexity of manufacturing the calibration object significantly.
- It should cover more area than the current calibration object. The calibration object's size was chosen such that, it will be completely included in the camera field of view in the experiments. However since multiple cameras were involved, the calibration object did not entirely cover the whole field of view in both images as we can see in Figure 3.11. It results in less accurate computation of the 3D coordinates. This problem can be overcome by having a larger calibration object, having larger number of vertices as discussed in the previous suggestion. Each vertex of the calibration object needs to be marked with numbers, which will help to identify each vertex easily.

### 3.6 Experimental verification

A femoral artery was dissected from a male Sprague Dawley rat and tested in the test setup. DLT calibration was applied and the real world 3D coordinates were calculated for five points on the artery. Stretch ratios  $\lambda_x$ ,  $\lambda_y$  and  $\lambda_z$  were calculated between these points in the reference image and final image.

Figure 3.14 (a) and (b) are the reference image and maximum stretch image of the blood vessel respectively in the Camera 1 view. Figure 3.14 (c) and (d) are the reference image and maximum stretch image of the blood vessel, respectively, in the Camera 2 view. The maximum stretch image is not the maximum stretch that was reached during the test. It was the maximum stretch at which the microspheres on the surface of the blood vessel were uniquely identifiable in the two different positions. The reason for this was the presence of too many microspheres in the images made it impossible to uniquely identify their location in more deformed state of the blood vessel. Another factor that contributed to the loss of clarity in the more deformed images was that the branched section of the blood vessel went out of focus due to the stretching. This happened because both the cameras were inclined at an angle of about 45 degrees to the plane of the test setup. So even though the motion of the blood vessel took place mostly in the horizontal plane, there was significant movement perpendicular to the image plane of both the cameras.

Figure 3.16 shows the camera1 view of the branched blood vessel with the a few points marked 1, 2, 3, 4 and 5, which were identified in both the camera views and in the maximum stretch images. There were some factors that limited the number of points that could be used. Due to the large number of microspheres in the images, it was difficult to uniquely identify particular microspheres in the corresponding images. The problem was compounded by the need to identify the same microspheres in the other camera view as well. Another factor that contributed to the limitation in the points that could be used was loss of clarity in the stretched images due to certain part of the blood vessel went out of focus during to the test. This happened because both the cameras

were inclined at an angle of about 45 degrees to the plane of the test setup. So even though the motion of the blood vessel took place mostly in the horizontal plane, there was significant movement perpendicular to the image plane of both the cameras. This led to the stretched images being gradually more unclear and limited the points that could be used. So only those features that could be clearly identified in all 4 views were used in the computations. DLT calibration was applied to compute the real world coordinates of those points. Then the stretch ratios  $\lambda_x, \lambda_y, \lambda_z$  were calculated between points 1-4, 4-2, 3-5, 4-3 and 2-5. Table 3.3 shows the stretch ratios  $\lambda_x, \lambda_y, \lambda_z$  for the above five pairs of points.

The XYZ coordinate system was based on the calibration object. The stretch ratios  $\lambda_x, \lambda_y$  and  $\lambda_z$  correspond to the X, Y and Z axes in the coordinate system attached to the calibration object. The availability of very few markers to do the stretch ratio computation limits the conclusion that can be drawn from these results. Following are some patterns, which can be observed in the results.

The  $\lambda_z$  values are not very reliable in the above results. This is because the variation in the estimated positions of the Z axis values is very small and within the margin of error. So the resulting stretch ratios values are completely random. As discussed in section 3.5.3, the accuracy of the Z axis values was reduced due to the calibration object used in the experiment, which had fewer vertices in the Z axis.

The  $\lambda_x$  and  $\lambda_y$  values display a pattern. The stretch ratios between points 2-5 and points 3-5 are higher than those between the other pairs of markers chosen. This seems to correspond to the fact that those markers are closer to the branch locations than the

other markers. The stretch ratio  $\lambda_x$  between the points 4-2 and 4-3 is negative which indicates a compression taking place behind the branch section.

The above results, even though encouraging, still need further investigation to do an assessment of the DLT method as an image analysis tool to calculate the stretch values of branched locations of blood vessels.

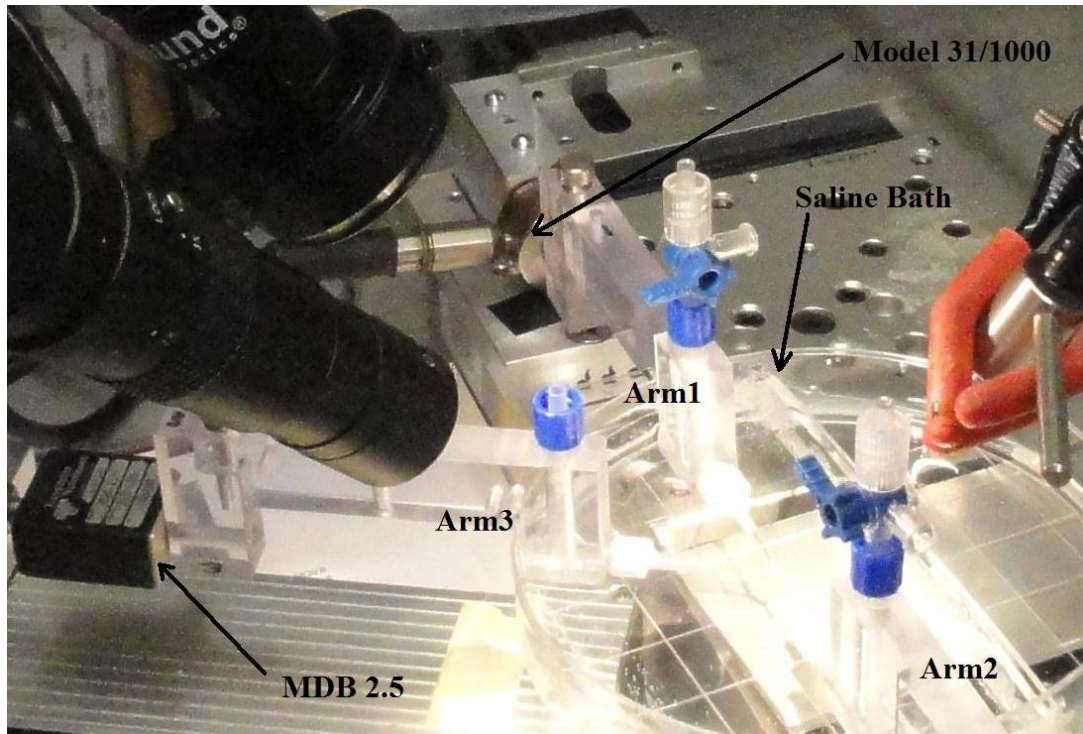


Figure 3.1. Branched vessel test setup

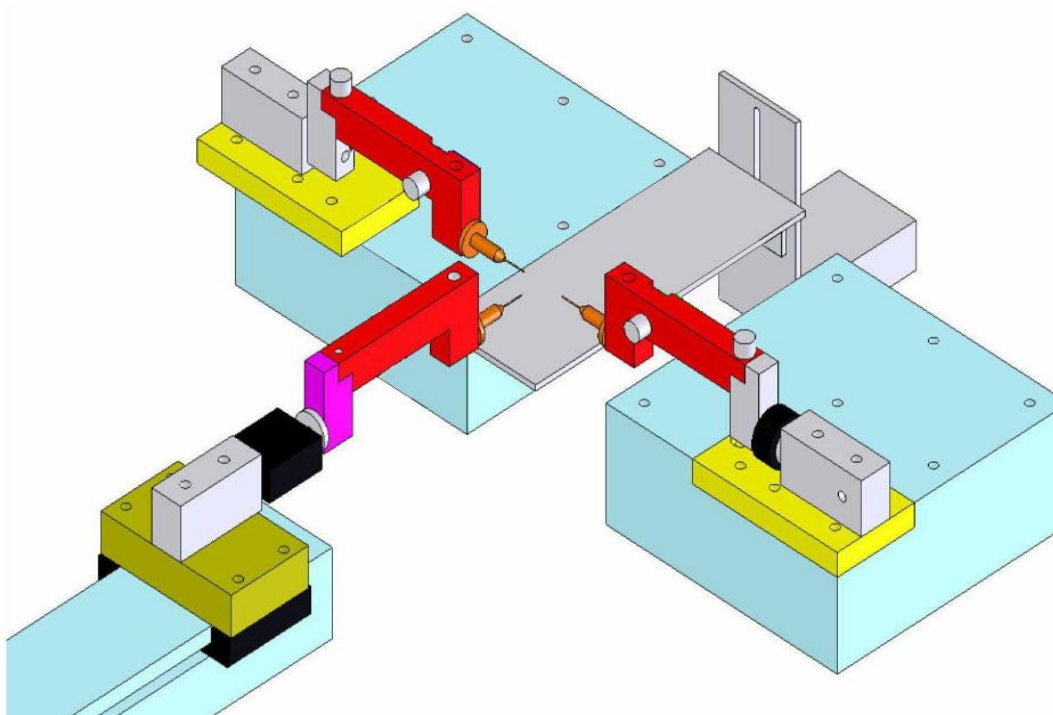


Figure 3.2. Diagrammatic representation of the branched vessel test setup



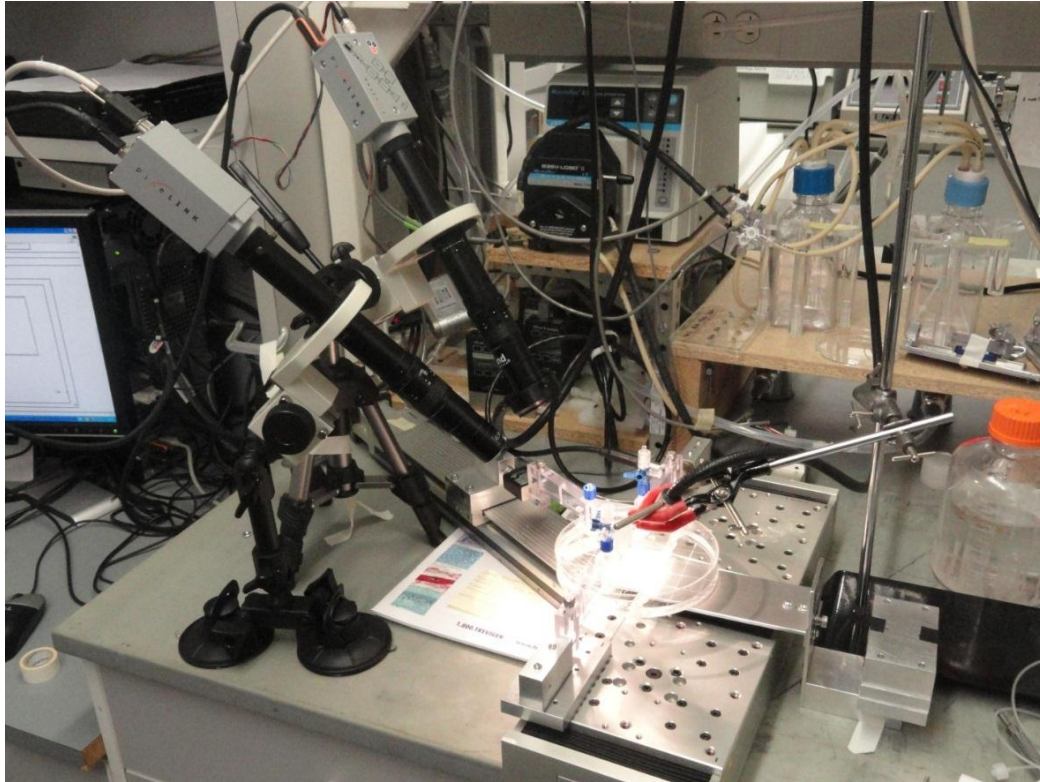


Figure 3.3. Branched vessel test setup showing the two cameras during a test

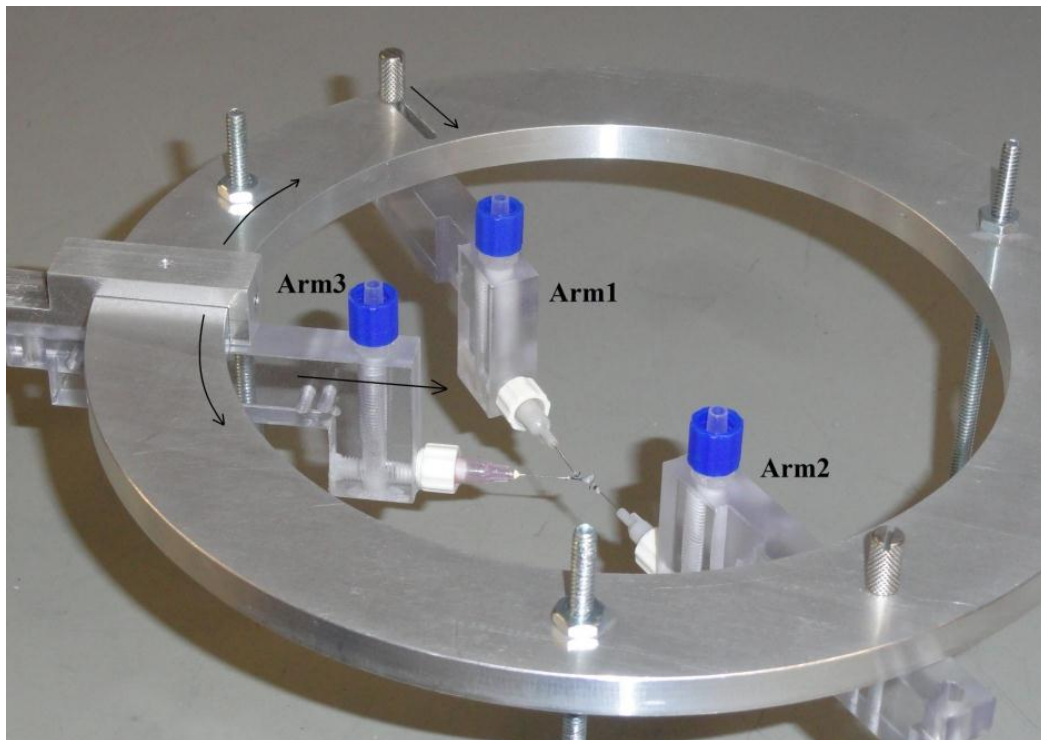


Figure 3.4. Branched vessel support arm fixture with the vessel attached

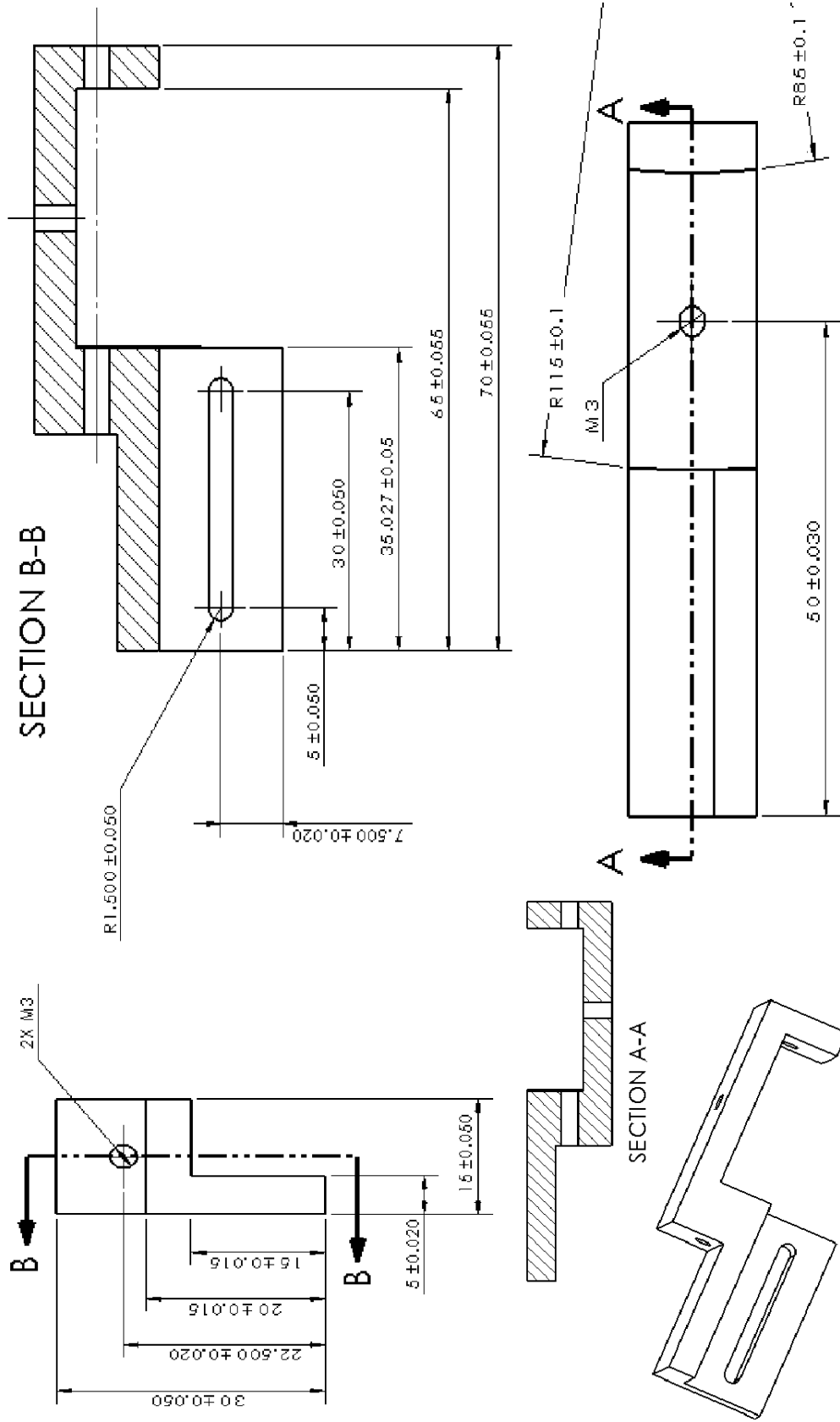


Figure 3.5(a). Drawings of the fixture

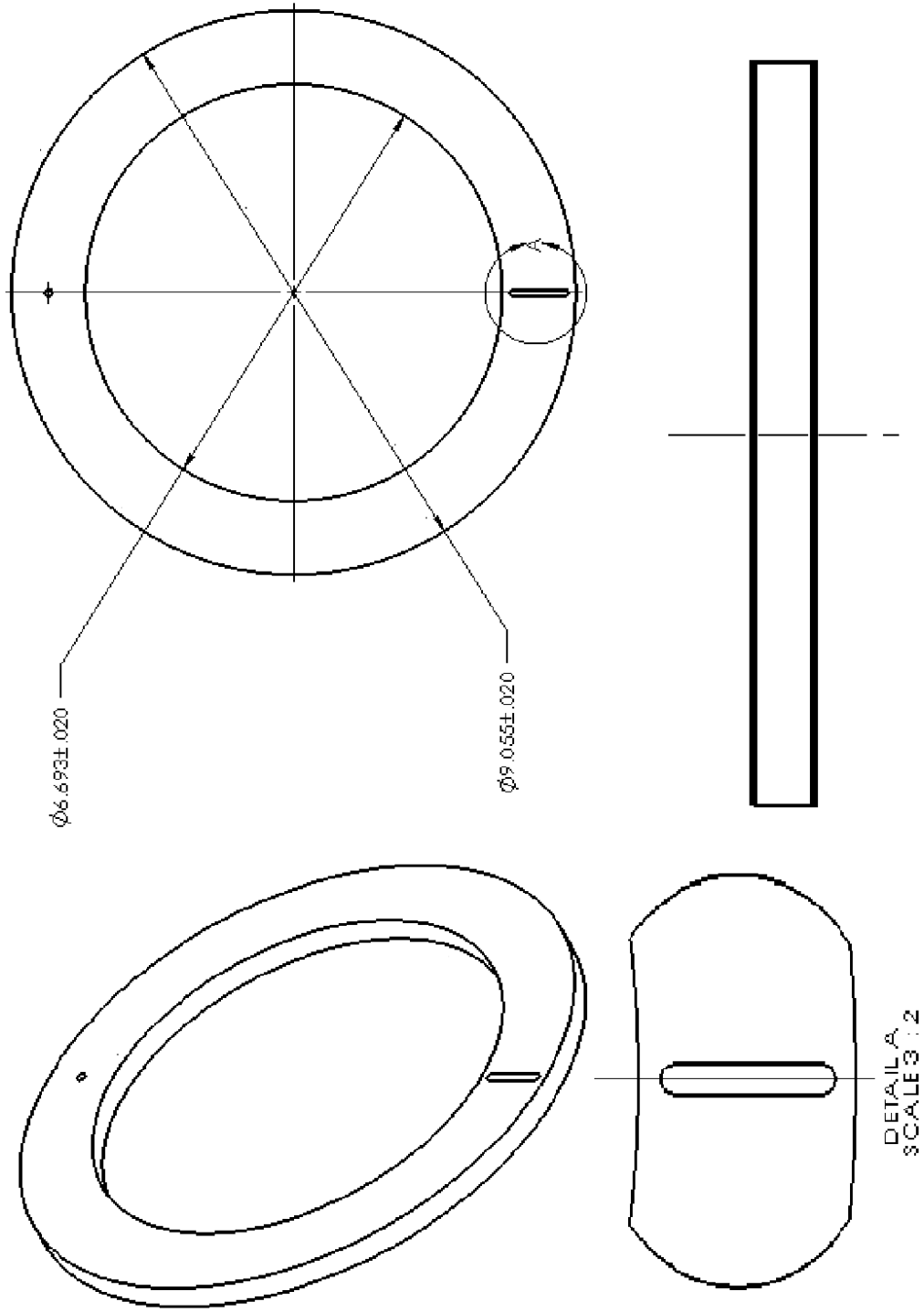


Figure 3.5(b). Drawings of the fixture

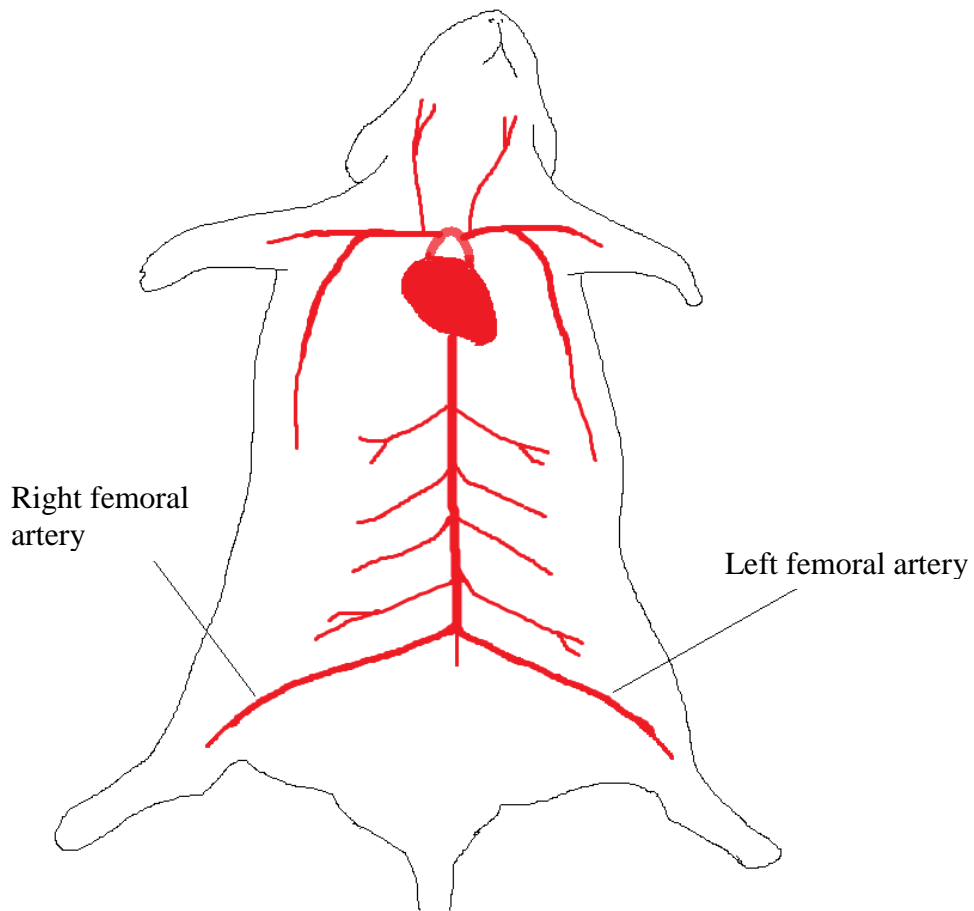


Figure 3.6. Diagrammatic representation of rat femoral arteries

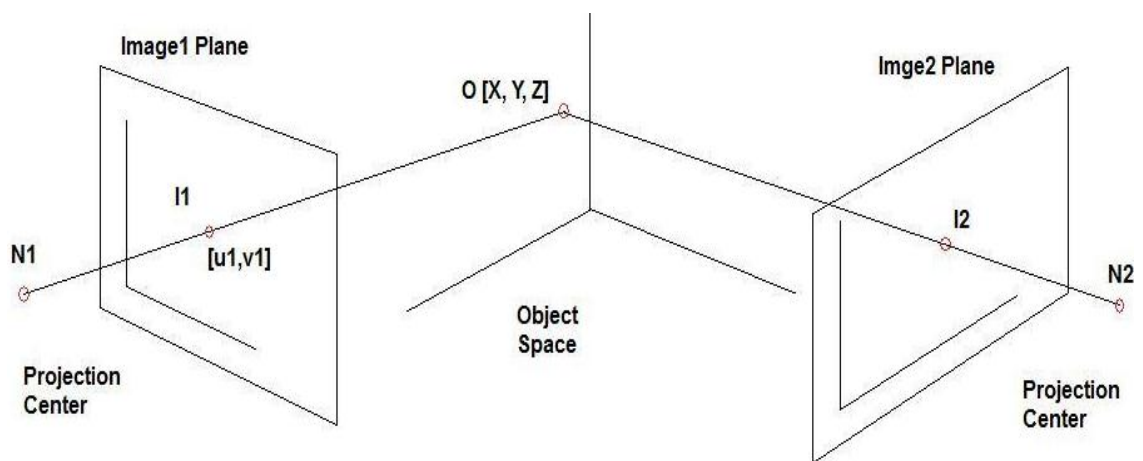


Figure 3.7. Object frame (XYZ-system) and Image frame (UV-system)

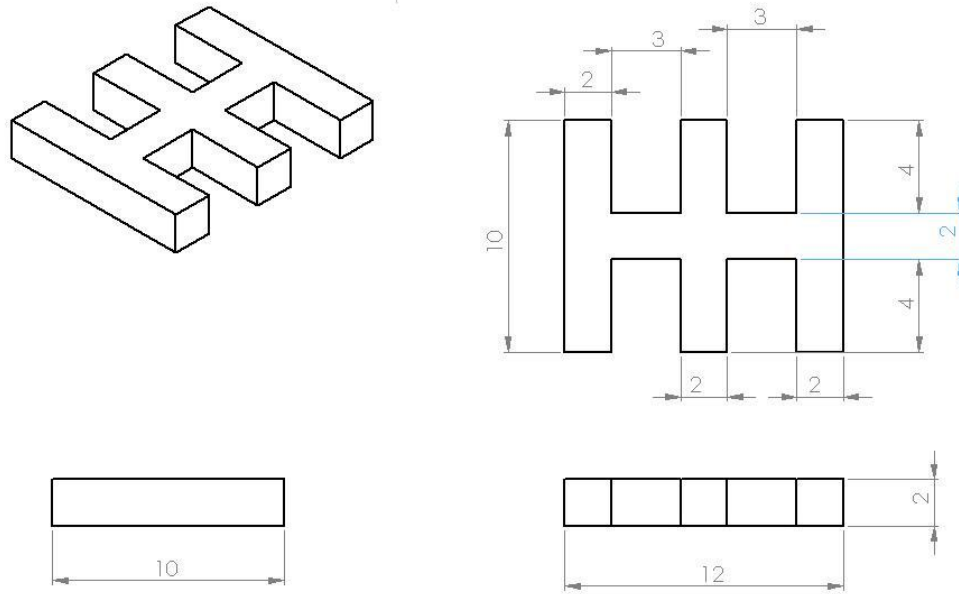


Figure 3.8. Drawing of the calibration object with the dimensions in millimeters

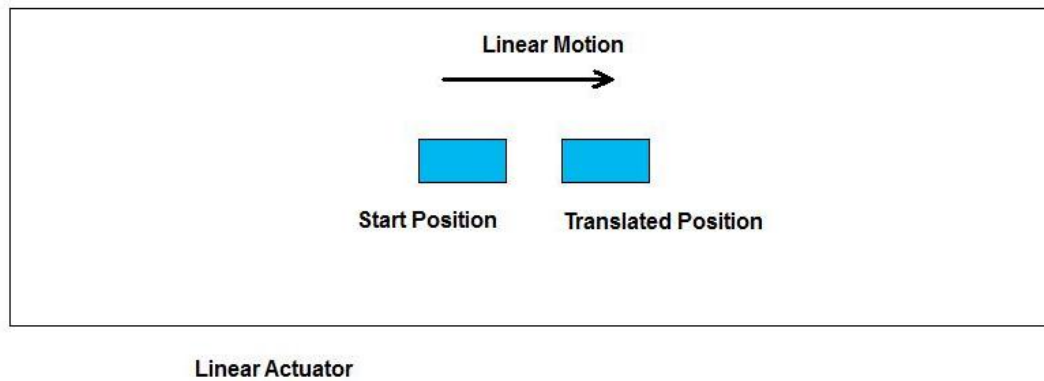


Figure 3.9. Linear DLT experiment schematic

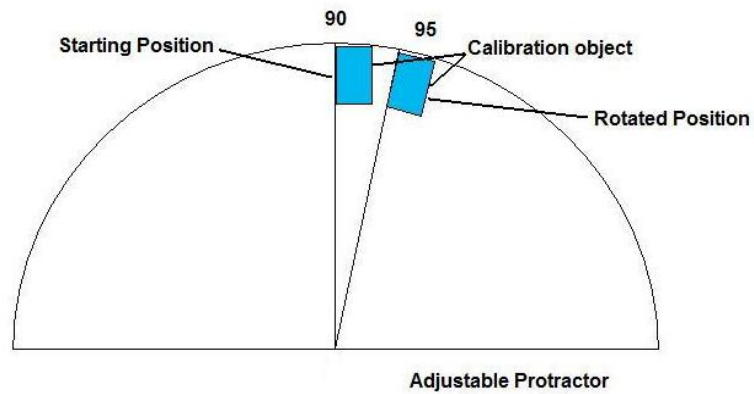


Figure 3.10. Rotational DLT experiment schematic



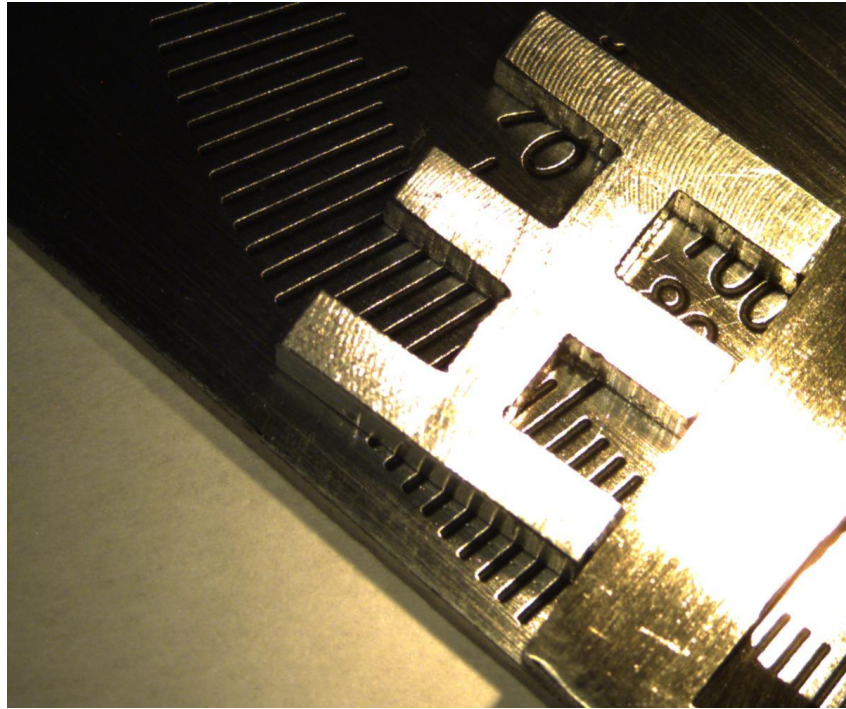


Figure 3.11. Calibration object kept on an adjustable protractor from Camera1

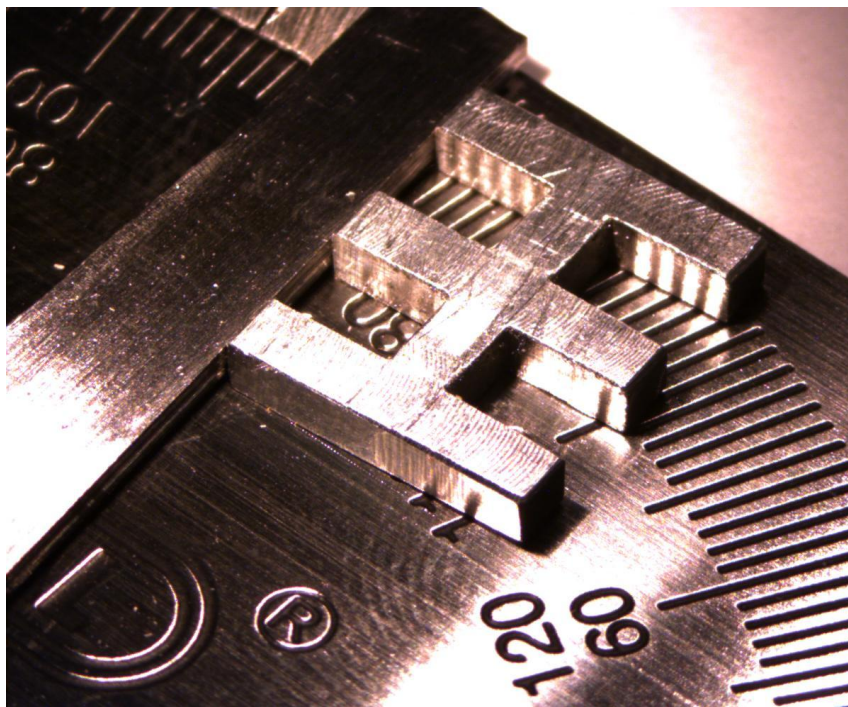


Figure 3.12. Calibration object kept on an adjustable protractor from Camera2

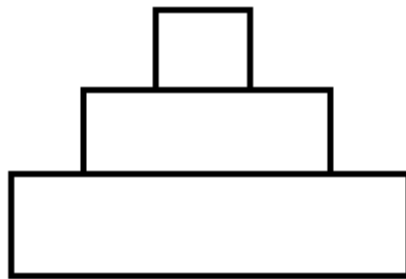


Figure 3.13. Proposed cross-section of the calibration object

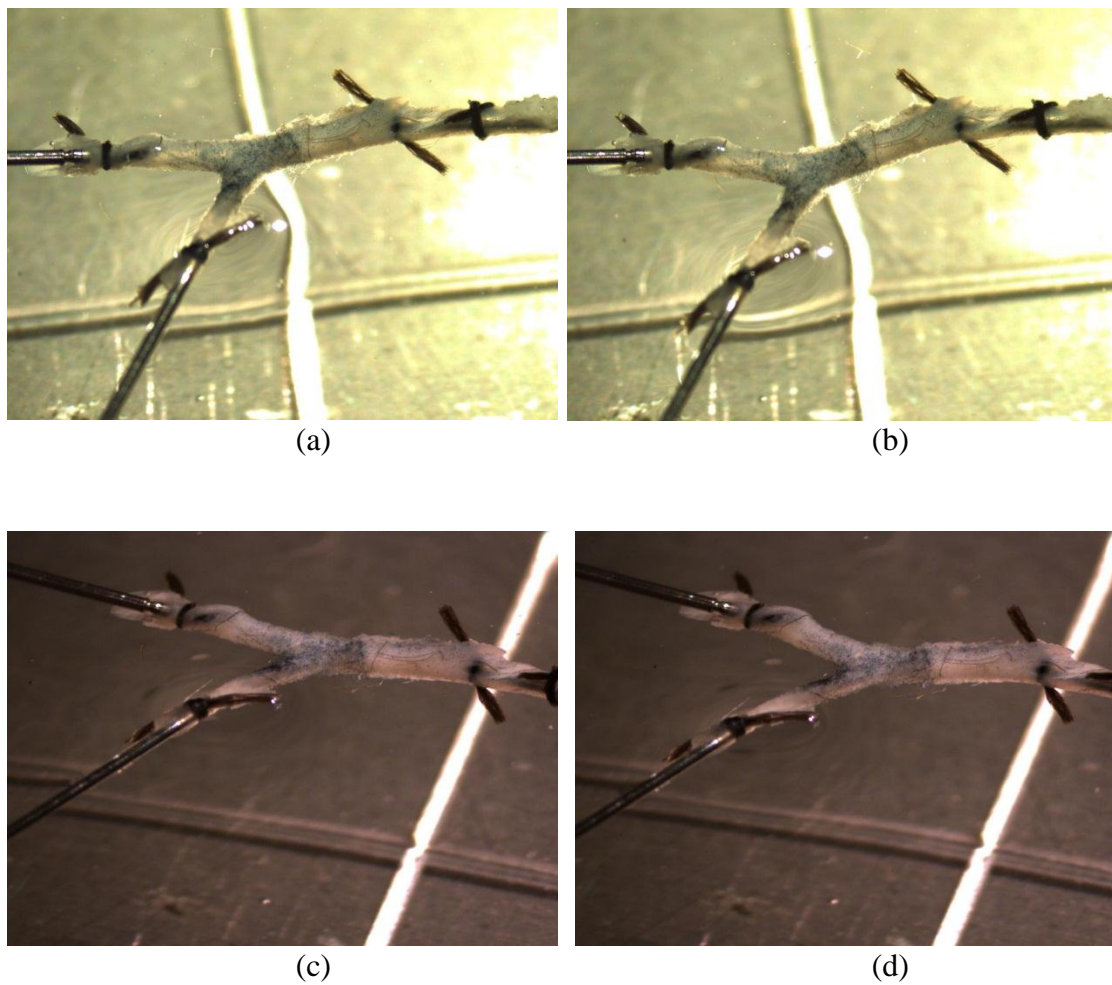


Figure 3.14. Rat femoral blood vessel (a) Camera1 reference image (b) Camera1 max stretch image (c) Camera2 reference image (d) Camera2 max stretch image



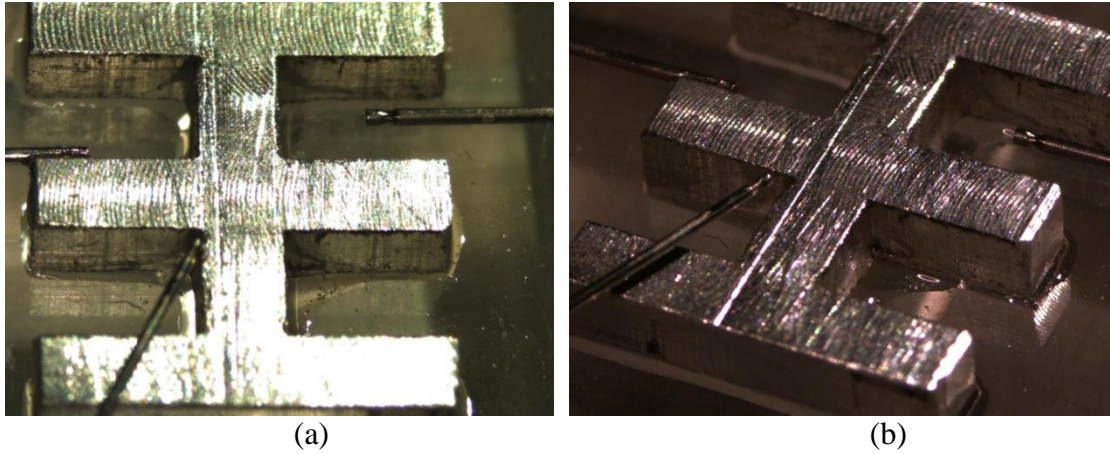


Figure 3.15. Calibration object (a) Camera1 image (b) Camera2 image

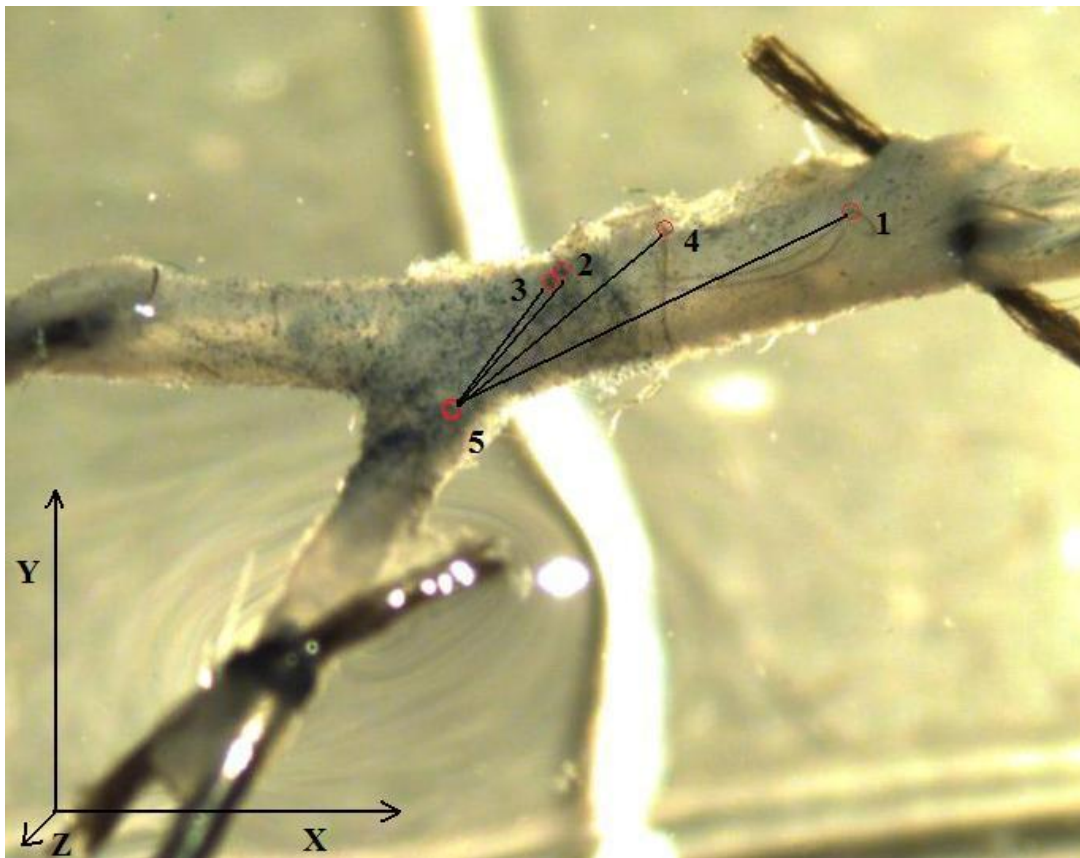


Figure 3.16. The points marked by the microspheres traced for the strain measurements



Table 3.1 Results of the linear DLT experiment

Real X	Real Y	Real Z	DLT X	% Error	DLT Y	% Error	DLT Z	% Error
0	5	2	-0.02	0.2	5.03	0.3	1.98	1
4	10	2	3.97	0.3	10.08	0.8	1.95	2.5
10	5	0	9.94	0.6	5.02	0.2	-0.04	2
6	10	0	5.96	0.4	10.13	1.3	-0.07	3.5

Table 3.2 Results of the rotational DLT experiment

Real X	Real Y	Real Z	DLT X	% Error	DLT Y	% Error	DLT Z	% Error
2.92	1.87	2	2.91	0.07	1.89	0.15	2.01	0.5
3.08	4.87	2	3.03	0.37	4.90	0.22	1.98	1
3.74	11.84	2	3.71	0.22	11.83	0.07	1.96	2
13.38	6.23	0	13.31	0.54	6.17	0.44	0.04	2

Table 3.3 Stretch ratios  $\lambda_x, \lambda_y, \lambda_z$  for the five pairs of points in figure 3.16

	$\lambda_x$	$\lambda_y$	$\lambda_z$
1-4	1.004	1.3129	0.4913
4-2	0.9578	1.3172	1.1696
3-5	1.3461	1.2480	1.3065
4-3	0.9254	1.2851	1.6406
2-5	1.2487	1.2466	1.5188

## CHAPTER 4

### SUMMARY AND FUTURE GOALS

The objective of this work was to develop and test a method to perform mechanical tests on branched blood vessels and collect more accurate data from the branch locations. Some modifications were made in the test setup hardware and software, to collect more accurate data from the branch locations. Another goal of these modifications was to streamline the testing process and decrease time needed to analyze of the data collected during the tests. The synchronization of the image acquisition with the data acquisition increased the accuracy of the results as each image could be correlated to the corresponding data points. It eliminated the need of manually comparing the images with the data during the post processing of the data, which is very time consuming and is prone to inaccuracy. The accuracy of the two camera Direct Linear Transformation (DLT) method also depended on triggering of both the cameras simultaneously. Integration of the calibration utility with the test-setup sped up the process of calibrating the camera and which helped to perform the experiment quickly. The image processing based automatic axial diameter measurement functionality enabled tracking the diameter during the tests for a prolonged period.

The fixture designed to mount the branched blood vessel on the arms of the test setup increased the ease with which it can be done. It also reduced the chance of

damaging the blood vessel and ensured the safe transport of the vessel from under the microscope to the test fixture. The DLT camera calibration technique proved to be an effective tool to compute the real world coordinates. However it has some limitations. Its accuracy depends heavily of the calibration object. The results from the experiment are encouraging and can be used as a background work for future experiments on branched blood vessels. However, certain improvements can be done for more accurate and detailed results. Following are some of the future goals.

A more accurate calibration object having more markers (especially in the **Z** direction) should be used to get a more accurate DLT calibration. A new calibration object can be designed as discussed in Chapter 3, which will aid more accurate computation of the Z axis coordinates and improve the reliability of the results.

The images collected in this experiment were unclear, which hindered tracking more points. A more accurate strain map can be built if more points can be tracked in the first and last image in both the camera views. The presence of a large number of microspheres in the above experiment hindered locating them distinctly. So use of a fewer number of microspheres could be helpful. A light source located below the specimen can also improve the resolution of the images.

## REFERENCES

1. Monson, K. L., and W. Goldsmith, 2003: Axial mechanical properties of fresh human cerebral blood vessels. *J. Biomech. Eng.*, **125** (2), 288-294.
2. Monson, K. L., N. B. Barbaro, and G. T. Manley, 2008: Biaxial response of passive human cerebral arteries. *Ann Biomed Eng.*, **36** (12), 2028-2041.
3. Mitchell, P., and J. Jakubowski, 2002: Failure testing cerebral arteries: are branch points weaker than unbranched vessels. *British Journal of Neurosurgery*, **16** (6), 578-582.
4. Rossitti, S., and J. Lofgren, 1993: Optimality principles and flow orderliness at the branching points of cerebral arteries. *Stroke*, **24**, 1029-1032.
5. Liou, T. M., T. W. Chang, W. C. Chang, 1994: Pulsatile flow through a bifurcation with a cerebrovascular aneurysm. *J. Biomech. Eng.*, **116** (1), 112-118.
6. Roach, M. R., 1986: The structure and elastic properties of arterial junctions. *Connective Tissue, Research*, **15** (1-2), 77-84.
7. Abdel-Aziz, Y. I., H. M. Karara, 1971: Direct linear transformation into object space coordinates in close range photography. *Proc. Symposium on close-range photogrammetry, Urbana*, **1**, 1-18.
8. Sid-Ahmed, M. A., and M. T. Boraie, 1990: Dual camera calibration for 3-D machine vision metrology. *IEEE Transactions on Instrumentation and Measurement*, **39** (3), 512-516.
9. Chen, L., C. W. Armstrong, and D. D. Raftopoulos, 1994: An investigation on the accuracy of three-dimensional space reconstruction using the direct linear transformation technique. *J. Biomechanics* **27** (4), 493-500.
10. MacKay, S. A., M. J. Potel, and J. M. Rubin, 1982: Graphics methods for tracking three-dimensional heart wall motion. *Computers and Biomedical Research*, **15**, 455-473.
11. Everett, W. N., P. Shih, J. D. Humphrey, 2005: A bi-plane video based system for studying the mechanics of arterial bifurcations. *Society of Experimental Mechanics*, **45** (4), 377-382.

12. Heikkila, J., O. Silven, 1997: A four-step camera calibration procedure with implicit image correlation. Washington, DC, IEEE Computer Society, *Computer Vision and Pattern Recognition, IEEE Computer Society Conference*, 1106–1112.
13. Melen, T., 1994: Extracting physical camera parameters from the 3 x 3 direct linear transformation matrix. Zurich, Switzerland, Armin Gruen, *Proc. SPIE*, 2252, 355-367.
14. Gruen, A., and T. S. Huang, 2001: *Calibration and orientation of cameras in computer vision*. 1st ed. Springer-Verlag, 231 pp.
15. Doehring, T. C., M. Kahelin, I. Vesely, 2009: Direct measurement of nonuniform large deformations in soft tissue during uniaxial extension. *J. Biomech. Eng.*, **131** (6), 061001 (6 pages), <http://dx.doi.org/10.1115/1.3116155>.
16. Smutz, W. P., M. Drexler, L. J. Berglund, E. Growney, K.N. An, 1996: Accuracy of video strain measurement system. *J. Biomechanics*, **29** (6), 813-817.
17. Crooks, D. A., 1991: Pathogenesis and biomechanics of traumatic intracranial hemorrhages. *Virchows Archive A: Pathological Anatomy*, **418** (6), 479-483.
18. Thurman, D. J., C. Alverson, K. A. Dunn, J. Guerrero, and J. E. Sniezk, 1999: Traumatic brain injury in the united States: A public health perspective. *J. Head Trauma Rehabil*, **14** (6), 602-615.
19. Genarelli, T. A., L. E. Thibault, A. K. Ommaya, 1972: Pathophysiologic responses to rotational and translational accelerations of the head. *SAE Technical Paper 720970*.
20. Ommaya, A. K., R. L. Grubb, and R. A. Naumann, 1971: Coup and contre-coup injury. *Journal of Neurosurgery*, **35** (5), 503-516.
21. Ommaya, A. K., F. Faas, and P. Yarnell, 1968: Whiplash injury and brain damage. *The Journal of American Medical Association*, **204** (4), 285-289.
22. Genarelli, T. A., and J. M. Abel, 1979: Differential tolerance of frontal and temporal lobes to contusion induced by angular acceleration. *SAE Technical Paper 791022*.
23. Genarelli, T. A., and L. E. Thaibault, 1982: Biomechanics of acute subdural hematoma. *The Journal of Trauma*, **22** (8), 680-686.
24. Lee, M. C, and R. C. Haut, 1989: Insensitivity of tensile failure properties of human bridging veins to strain rate: Implications in biomechanics of subdural hematoma. *Journal of Biomechanics*, **22** (6-7), 537-542.

25. Furin, A. H., G. H. Juhl, and C. Taylor, 1984: Interhemispheric subdural hematoma. *Journal of Neurosurgery*, **60** (6), 1300-1302.
26. Young-Hoo Kwon, cited 1998: DLT method. [ Available online at <http://www.kwon3d.com/theory/dlt/dlt.html>.]